Driving Flows in Laboratory Astrophysical Plasma Jets: The Mochi.LabJet Experiment

Evan G. Carroll

A thesis
submitted in partial fulfillment of the
requirements for the degree of

Master of Science in Aeronautics & Astronautics

University of Washington

2016

Committee:
Setthivoine You
Ray Golingo

Program Authorized to Offer Degree:
Aeronautics & Astronautics

University of Washington

Abstract

Driving Flows in Laboratory Astrophysical Plasma Jets:
The Mochi.LabJet Experiment

Evan G. Carroll

Chair of the Supervisory Committee:
Assistant Professor Setthivoine You
William E. Boeing Department of Aeronautics & Astronautics

Mochi.Labjet is a new experiment at the University of Washington developed to investigate the interaction of shear flows in plasma jets with boundary conditions similar to an accretion disc system. This thesis details the engineering design and first plasmas of the Mochi.Labjet experiment. The experiment required construction of a new three electrode plasma gun with azimuthal symmetric gas injection, two optically-isolated pulsed power supplies for generating and sustaining plasma, and one optically-isolated pulsed power supply for generating a background magnetic field. Optical isolation is achieved with four custom circuits: the TTL-optical transmitter, optical-TTL receiver, optical-relay, and optical-tachometer circuits. First plasmas, during the commissioning phase of the apparatus, show evidence of flared jet structures with significant azimuthal symmetry.

Table of Contents

List of Figures iii

Chapter 1 - Introduction 1

1.1 Astrophysical Jets in the Laboratory 2

1.2 The Mochi.Labjet Experiment 6

1.2.1 The Mochi.LabJet Plasma Gun 7

1.2.2 Gun Electrode Pulsed-Power Supply Unit 8

1.2.3 Magnetic Field Pulsed-Power Supply Unit 10

Chapter 2 - Mochi.LabJet Plasma Gun 12

2.1 Inner Electrode 13

2.2 Middle Electrode 14

2.3 Outer Electrode 16

2.4 Gas Plume Model 17

Chapter 3 – Electrode Power Supply Units 19

3.1 High Speed Power Electronics 19

3.2 Mochi.LabJet PSU2 and PSU3 Overview 21

3.3 Custom Ignitron Tower 23

3.4 Circuit Simulation 27

3.5 Low Voltage Optically-Isolated Control Electronics 30

3.5.1 TTL-Optical Transmitter Circuit 31

3.5.2 Optical-TTL Receiver Circuit 32

3.5.3 Optical-Relay Circuit 34

3.5.4 Optical-Tachometer Circuit 36

Chapter 4 – First Plasmas 39

4.1 Flared Plasma Jet 39

4.2 The Bundt Cake Formation 43

Chapter 5 – Conclusion 45

Bibliography 47

Appendix A – Mochi.LabJet.Gun 49

A.1 Mochi.Labjet.Gun Assembly 49

A.2 Mochi.LabJet.Gun Inner Electrode Assembly 51

A.3 Mochi.LabJet.Gun.MiddleElectrode Assembly 53

A.4 Mochi.LabJet.Gun.Outer.Electrode Assembly 55

A.4.1 Mochi.LabJet.Gun.OuterElectrode.InnerPlenum Assembly 57

A.4.2 Mochi.LabJet.Gun.OuterElectrode.OuterPlenum Assembly 59

Appendix B – Mochi.LabJet.PSU 61

B.1 Mochi.LabJet.PSU.IgnitronTower 61

B.2 Mochi.LabJet.PSU.CapacitorBank Assembly 63

List of Figures

Figure 1 – Radio Galaxy Cygnus A. 1

Figure 2 – Boundary Conditions of an Astrophysical Jet. 4

Figure 3 – Caltech Plasma Evolution. 5

Figure 4 – Three Electrode Plasma Gun Configuration (Chapter 2). 7

Figure 5 – Curves of Paschen's Law for Select Gases. 9

Figure 6 – The Mochi.LabJet Plasma Gun. 12

Figure 7 – Inner Electrode Assembly. 13

Figure 8 – Inner Electrode Gas Injection. 14

Figure 9 – The Middle Electrode Assembly. 15

Figure 10 – Middle Electrode Gas Injection. 15

Figure 11 – Outer Electrode Assembly. 16

Figure 12 – Gas Plume Model. 18

Figure 13 – Gun Electrode Power Supply Circuit Diagram. 22

Figure 14 – Gun Electrode Power Supply Unit. 23

Figure 15 – Gun Electrode Power Supply Capacitor Bank and Custom Ignitron Tower. 24

Figure 16 – PSU QUCS Circuit Simulation. 27

Figure 17 – Plot of PSU QUCS Simulation Output. 30

Figure 18 – TTL-Optical Transmitter Circuit. 32

Figure 19 – Optical-TTL Receiver Circuit. 33

Figure 20 – Optical-TTL Reciever Circuit Switching Times. 34

Figure 21 – Optical-Relay Circuit. 35

Figure 22 – Optical-Relay Switching Times. 36

Figure 23 – Optical-Tachometer Circuit. 37

Figure 24 – Optical-Tachometer Circuit Performance. 38

Figure 25 – Votlage Traces for Shots 3080-3091. 39

Figure 26 – Current Traces for Shots 3080-3091. 40

Figure 27 – Time Evolution of Flared Plasma Jet. 41

Figure 28 - Current Comparison of Shot 3085 with QUCS Simulation. ……..42

Figure 29 - Bundt Cake Formation. ……43

Acknowledgments

First and foremost, I would like to thank my parents and my brother for their absolute love and support.

I would like to thank Alex Card for always having my back and straightening me out when I needed it. He is a knowledgeable colleague, a genuine person, and a valuable friend. I will never forget our spirited motorcycle rides around Seattle.

I would like to thank Eamon McQuaide and Reginald Rocamora for their patience and expertise in the mechanical engineering annex machine shop. Their consultation was invaluable during the couple thousand hours I spent in that shop - and most certainly, critical to my success. They are always friendly, willing to help, and have put up with all of my shenanigans. Some of the most relaxing times I have had in graduate school were making chips while listening to Ethio-jazz.

I would like to thank Setthivoine You for allowing me the opportunity to participate in his research group. Sett took a leap of faith bringing me on as a new graduate student with no background in plasma physics, electrical engineering, or experimental research. He allowed me tremendous freedom and responsibility on projects that were crucial for the lab's success - a rare experience for most graduate students. I was able to make mistakes, be creative, take risks, and show what I am truly capable of. His passion is infectious and his vision is inspiring; I feel very lucky to have been a part of it.

And finally, I would like to thank Liz and Makaio Lopez for making it all worth it.

Dedication

To my parents, Steve and Jacquie.

Chapter 1 - Introduction

Highly collimated outflows from accretion disc systems (Figure 1), commonly referred to as astrophysical jets, are some of the largest structures in the known universe, varying from a few light years to millions of parsecs in length. These jets dwarf their central object and accretion disc and outflow velocities vary from ~100 km/s in proto-stellar jets to significant fractions of the speed of light in active galactic nuclei [1]. Despite varying many orders of magnitude, these jets exhibit similarity in their source regions: dense central object, high speed disc of accreting matter, and a dipole background magnetic field linking the two.

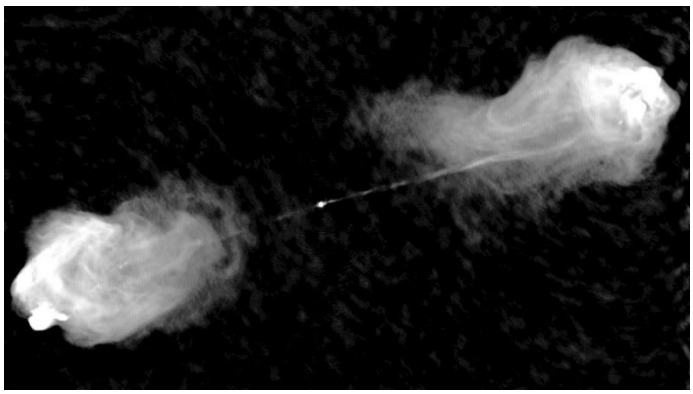

Figure 1 - Radio Galaxy Cygnus A. Highly collimated bi-polar outflows erupt from an accretion disc system and terminate into stagnated radial lobes. Image: courtesy of NRAO/AUI http://images.nrao.edu/261.

The mechanisms that launch, sustain and collimate these jets are not fully understood. In the past, they were assumed to be described by purely hydrodynamic models; however, recent observations of helical magnetic fields in jets suggest axial currents [2] and confirmed speculation [3] that the dynamics of these structures were driven by plasma physics. Because of the length and time scales involved, it is impossible to recreate full scale astrophysical plasmas in a laboratory setting. However, common plasma models such as magnetohydrodynamics (MHD) have no

intrinsic scale lengths, thus the dynamics of astrophysical plasmas could be interpreted from laboratory plasmas with sufficient fidelity.

1.1 Astrophysical Jets in the Laboratory

To compare any two systems, despite wide variation in spatial and temporal scale, requires the governing equations that describe their dynamics to be invariant. The equations of Ideal MHD do not have explicit dependence on scale lengths. Thus, scaling relations can be derived with a change of variables, which can be used to relate laboratory plasmas to astrophysical plasmas. The Ideal MHD equations [4]

$$\rho\left(\frac{\partial\vec{v}}{\partial t}+\vec{v}\cdot\nabla\vec{v}\right)=-\nabla p-\frac{1}{4\pi}\vec{B}\times\nabla\times\vec{B} \tag{1.1}$$

$$\frac{\partial\rho}{\partial t}+\nabla\cdot\rho\vec{v}=0 \tag{1.2}$$

$$\frac{\partial\vec{B}}{\partial t}=\nabla\times\left(\vec{v}\times\vec{B}\right) \tag{1.3}$$

where ρ is density, $\vec{v}$ is velocity, p is pressure, $\vec{B}$ is magnetic field and t is time, describing two systems are invariant as long as the following scaling relations are satisfied [5]:

$$\vec{r}=a\vec{r}_1 \tag{1.4}$$

$$\rho=b\rho_1 \tag{1.5}$$

$$p=cp_1 \tag{1.6}$$

$$\vec{v}=\sqrt{\frac{c}{b}}\vec{v}_1 \tag{1.7}$$

$$\vec{B}=\sqrt{c}\,\vec{B}_1 \tag{1.8}$$

$$t = a\sqrt{\frac{b}{c}}\, t_1 \tag{1.9}$$

where $\vec{r}$ is scale length and the subscript denotes the scaled system. Therefore, dynamics of astrophysical plasma jets can be inferred from laboratory simulations as long as both systems satisfy these scaling relations and the assumptions of MHD.

In general, there are two different approaches to simulating astrophysical jets in the laboratory. The first, is to try to replicate as many dimensionless parameters as possible, such as the Mach and Lundquist number, while disregarding the details of the formation region. For example, an experiment at Imperial College generates 1 MA current through a radial wire array between two electrodes and generates jets with Mach number, plasma beta and cooling parameter similar to proto-stellar jets; however, does not replicate the boundary conditions of an accretion disc system [6]. From an experimental design viewpoint, this method is advantageous because the source region spins up to small fractions of the speed of light, and is not feasible to replicate in a laboratory. A disadvantage of this method is that the justification of relevance to astrophysical phenomena depends solely on matching any and all dimensionless parameters. Furthermore, even if a laboratory jet could match every dimensionless parameter, it cannot be completely convincing because it excludes details observed in nature.

The second approach, involves simulating equivalent boundary conditions of the jet and its formation region, without achieving the exact values of dimensionless parameters. Figure 2 shows the boundary conditions of an astrophysical jet and accretion disc system. Because of the wide variation of dimensionless parameters in real astrophysical jets, it is possible that the similar boundary conditions maybe more important to launching and sustaining these structures. Previous work at Caltech showed that concentric co-planar two electrode plasma guns mimic the boundary

conditions of magnetically driven plasma jets launched from accretion disc systems such as young stellar objects and active galactic nuclei [7].

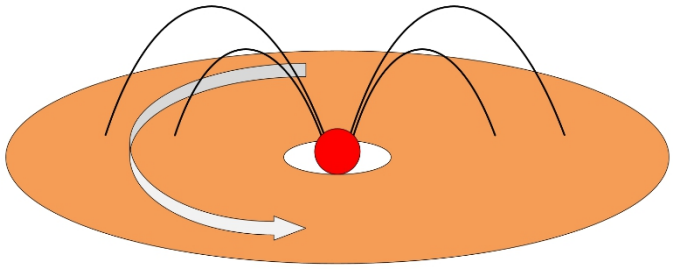

Figure 2 – Boundary Conditions of an Astrophysical Jet. A thin accretion disc (orange annulus) rotating around a compact central object (red sphere) is threaded with a poloidal magnetic field (black lines).

In concentric co-planar plasma guns, two electrodes, a disc and an annulus, represent the central object and the accretion disc. When biased at different potentials a radial electric field is established between the gaps in the electrodes. A background magnetic field generated from an external solenoid, links the electrodes similar to the magnetic field linking the central object to the accretion disc. According to Ohm's Law of Ideal MHD [8]

$$\vec{E} = -\vec{v} \times \vec{B}, \tag{1.10}$$

a radial electric field is equivalent to rotation of an accretion disc perpendicular to a background poloidal magnetic field

$$\vec{E} = -v_\phi \vec{\phi} \times B_z \vec{z} = -v_\phi B_z \vec{r} \tag{1.11}$$

where v_ϕ is the magnitude of the tangential velocity at a point on the accretion disc and B_z is the background magnetic field. Gas is injected from discrete locations on each electrode. Dense plasma arches form along the poloidal field lines resembling spider legs. Electromagnetic forces cause the arches to attract, collapsing into a central flared plasma jet that continues to collimate. A time evolution of the Caltech plasma jet is shown in Figure 3.

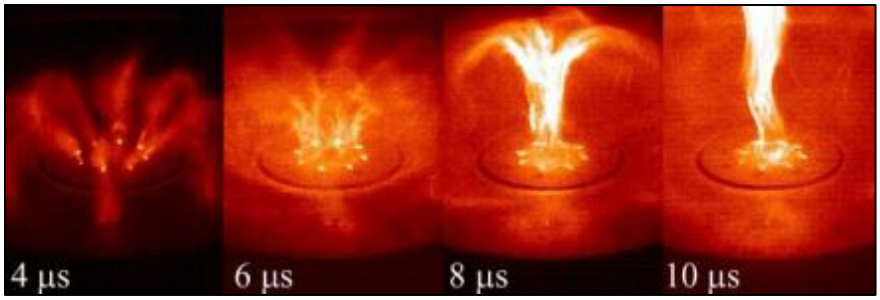

Figure 3 – Caltech Plasma Evolution. Dense plasma arches develop along background dipole magnetic field, and collapse into a jet on axis. Image: courtesy of Setthivoine You.

There has been experimental evidence [9], along with analytic theory [10], to suggest that the collimation of these plasma jets is a result of non-conservative MHD forces driving axial flows in a generalized, initially flared magnetic-flux tube with axial currents. Plasma and magnetic flux is convected to regions of lower magnetic field and stagnates, which increases the azimuthal magnetic flux density, thus increasing the radial self-pinch force. There is strong observational confirmation of this in plasma jets that terminate collimated flows into stagnated lobe regions (Figure 1). However, collimated magnetic flux tubes are susceptible to a current-driven MHD instability, called the "kink" instability, which disrupts the lengthening of these flux tubes by breaking up the plasma and halting current flow. Kruskal and Shafranov first identified the condition for the kink instability in a static, infinitely-long cylindrical plasma with the definition of the safety factor [11]

$$q(a) = \frac{2\pi a B_z(a)}{L B_\phi(a)} < 1 \tag{1.12}$$

where a is the radius of plasma, $B_z(a)$ is the axial magnetic field, L is the length of the plasma, and $B_\phi(a)$ is the azimuthal magnetic field. From equation 1.12, high aspect ratios $L/a > 1$, and or

large axial currents $B_z(a)/B\phi(a) < 1$, lead to kink instabilities, both of which occur during the collimation process of current-driven magnetic flux tubes.

The Caltech astrophysical jet experiment showed collimation of jets to aspect ratios of about 10:1 before kink instabilities occurred [12]. However, observed astrophysical jets seem to exhibit larger aspect ratios, suggesting that there are other mechanisms responsible for mitigating the kink instability and allowing further collimation. Recent developments have shown that axial shear flows will stabilize pressure driven instabilities in Z-Pinch plasmas, and jets with aspect ratios of about 30:1 have been observed on the ZaP experiment at the University of Washington [13]. However, the ZaP plasma has two fixed boundaries, which does not replicate the single fixed boundary tied to the central object of an accretion disc system. Although large velocities, ~50 km/s, were measured on the Caltech experiment [14], the configuration did not allow for sufficient shear flows to stabilize the current driven instabilities. Questions arise as to whether or not collimation and stabilization mechanisms can work in unison to produce jets with greater aspect ratios.

1.2 The Mochi.Labjet Experiment

Mochi.Labjet is a new experiment developed to investigate the interaction of shear flows in plasma jets with boundary conditions similar to an accretion disc system. The experiment required construction of a new plasma gun, two pulsed-power supplies for generating and sustaining plasma, and one pulsed-power supply for generating a background magnetic field.

1.2.1 The Mochi.LabJet Plasma Gun

The Mochi.LabJet plasma gun is similar to the coaxial planar plasma gun configuration from Caltech [7], but has three electrodes and azimuthally symmetric gas injection (Figure 4a). The inner and middle electrodes are biased at different voltages with respect to the outer electrode. A solenoid from behind the electrodes generates a dipole magnetic field, linking both the middle and inner electrode to the outer electrode. Gas is injected from custom gas valves [14] to slits in the electrodes with custom stacked plenums that allow for azimuthal symmetry. Unlike the two electrode configuration, three electrodes establishes two different radial electric fields, which according to Ideal Ohms Law (eq. 1.11), replicates two separate rotation velocities in an astrophysical accretion disc. The two separate rotation velocities create a sheared profile that could stabilize the jet from kink instabilities similar to flow stabilization theory [13]. Additionally, azimuthally symmetric gas injection may allow for stronger E × B rotation of the formation region and the final jet.

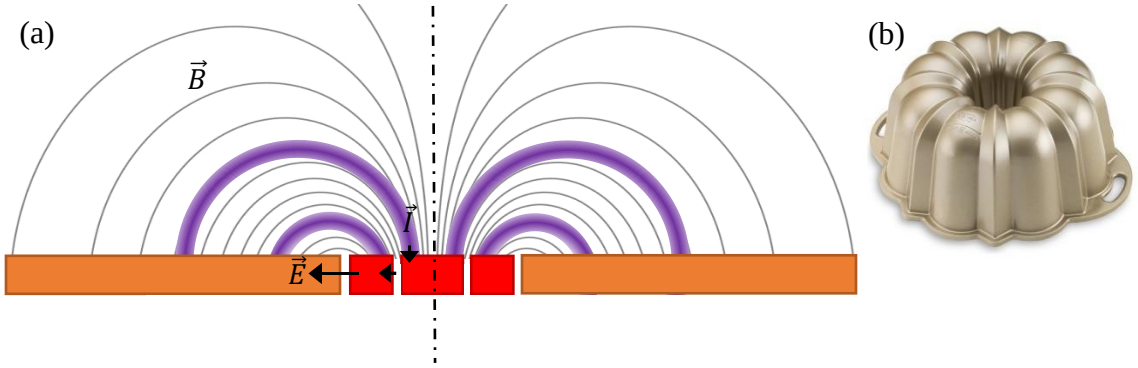

Figure 4 –Three Electrode Plasma Gun Configuration (Chapter 2). (a) During breakdown, azimuthally continuous plasma arch structures (purple) develop along the background magnetic field lines (gray), linking the inner (red) and middle electrodes (red) to the outer electrode (orange). (b) The formation (purple arches) resembles a Bundt cake pan. Image: courtesy of Houzz http://www.houzz.co.uk/photos/42190643/nordic-ware-anniversary-bundtr-pan-williams-sonoma-cake-tins.

The breakdown process in the three electrode configuration is similar to the two electrode configuration with the exception that the initial plasma arches are azimuthally continuous, rather than discrete, resembling two nested Bundt cake pans (Figure 4b). Because of this resemblance, the early stages in breakdown have been named the "Bundt cake formation." The inner regions of the two nested Bundt cake plasmas are pulled together from electromagnetic forces, while the outer regions are pushed apart, and a central jet forms on axis. The plasma jet's self-generated magnetic field combined with the background poloidal field produces helical magnetic fields with pitch that varies with the radial current density profile. Further details of the three electrode co-planar plasma gun are found in the Chapter 2.

1.2.2 Gun Electrode Pulsed-Power Supply Unit

The required voltage and current parameters that the power supplies need to generate are largely determined by plasma breakdown. The breakdown characteristics of the triple electrode gun can be approximated from Paschen's Law [15]. Paschen's Law describes the minimum voltage needed for a Townshend breakdown of neutral gas between two electrodes. The minimum breakdown voltage $\mathbf{V_B}$

$$V_B = \frac{Bpd}{\ln(Apd) - \ln\left(\ln\left(1 + \frac{1}{\gamma_{se}}\right)\right)} \tag{1.13}$$

is dependent on gas species and material of the electrodes, where p is the neutral gas pressure, d is the electrode distance, γ_{se} is the secondary electron emission coefficient, A and B are empirically determined coefficients related to the excitation and ionization energies of the gas species. Figure 5 plots Paschen's Law for some typical gases common to plasma experiments.

For each gas, there is an absolute minimum for breakdown at a specific pd, which for most gases is of the order of $10^2 - 10^3$ V. Because plasmas are good conductors, typical impedances and currents of laboratory plasmas are on the order of < 100 mΩ and $10^4 - 10^5$ A, respectively. The minimum power required for breakdown and sustainment is on the order of $V^2/R = 10^5 - 10^6$ W. Because of the extremely large power requirement, DC operation is not feasible, and a capacitor-based, pulsed-power solution has been developed. Further details of the gun electrode pulsed-power supply units are found in Chapter 3.

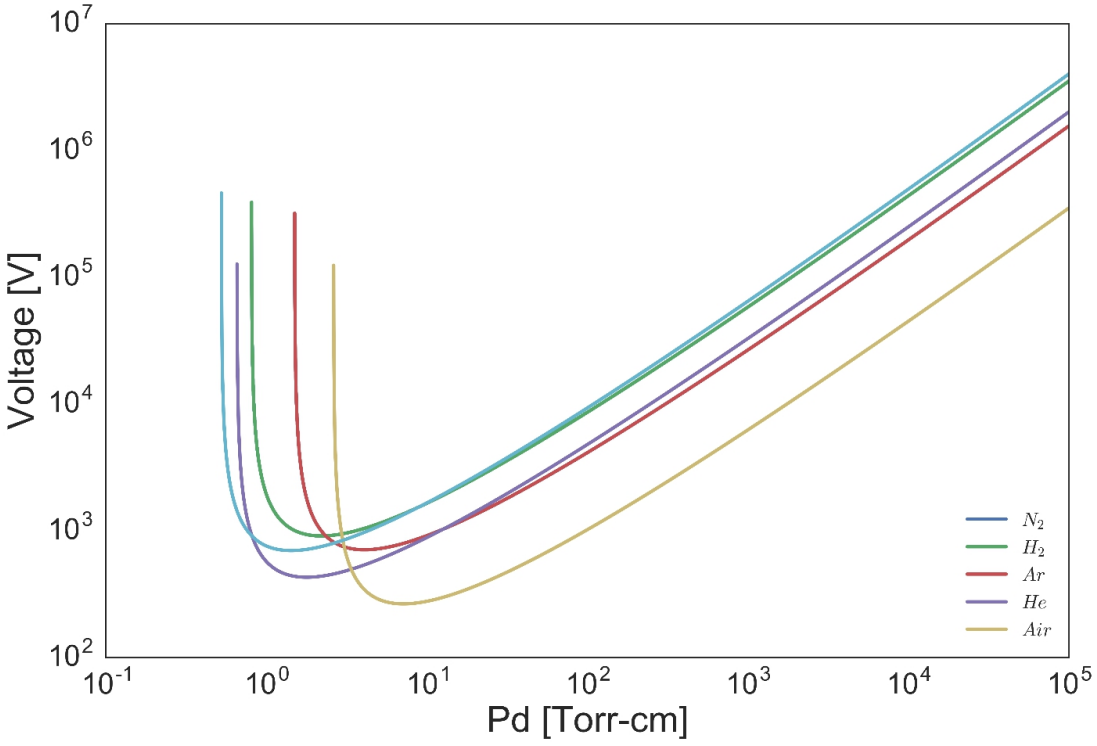

Figure 5 – Curves of Paschen's Law for Select Gases.

Additionally, there is an upper and lower limit for breakdown that corresponds to a high and low pressure regime. To the right of the high pressure limit, the mean free path between collisions is short, and any free electrons from ionization quickly lose energy due to collisions and

cannot propagate the breakdown. To the left of the low pressure limit, the mean free path is large, and very few collisions with neutral gas occur. When designing high-voltage hardware for use in vacuum, reducing the spacing of two conductors will increase the required breakdown voltage, which is the opposite intuition of daily experiences in atmospheric pressure. For the Mochi.LabJet experiment, the distance d can be defined as the arc-length of the magnetic field that links the electrode gas plenum exits. The Pd value is not constant due to the non-uniform gas distribution as it expands into vacuum. Additional detail of the non-uniform gas distribution can be found in Section 2.4.

1.2.3 Magnetic Field Pulsed-Power Supply Unit

The required background magnetic field strength is determined by the stability space set by the Kruskal-Shafranov limit. The magnetic field strength needs to vary, so that shear flows can stabilize jets to aspect ratios that were previously defined as kink unstable - jet currents of 10-100 kA require magnetic field strengths of 10-100 mT. The magnetic field power supply is nearly identical to the gun electrode power supplies (Chapter 3) with the exception that it contains six hundred 1 mF electrolytic capacitors in parallel and is switched by SCR. The magnetic field power supply is discharged through a custom solenoid – 100 windings of 4 mm square magnet wire with an inner and outer diameter of 2.75 in. and 6 in., respectively. The equivalent capacitance and total impedance in the power supply and solenoid produces underdamped RLC discharges with the first current peak (~600 A at 100V) occurring in 25 ms, orders of magnitude longer than a typical plasma duration. On the plasma time scale of 10-50 μs, the magnetic field generated from the solenoid is approximately constant. The magnetic field power supply is fired 25 ms prior to firing the gun electrode power supplies to allow the field to

soak into the electrodes and so that the plasma duration takes place at peak background magnetic field strengths. Although, the background magnetic field power supply was developed for the Mochi.LabJet experiment, further details are not discussed in this thesis.

Chapter 2 - Mochi.LabJet Plasma Gun

The Mochi.LabJet plasma gun (Figure 6) consists of 4 sub-assemblies: the inner electrode assembly (Section 2.1), the middle electrode assembly (Section 2.2), the outer electrode assembly (Section 2.3) and the high-voltage connection assembly (Appendix A.1). All four assemblies mount to an end-dome door on the Mochi vacuum chamber (Figure 6b), an electro-polished spherical stainless steel sphere, approximately 1.4 meters in diameter. The Mochi vacuum chamber is roughed by an Edwards XDS-10 scroll pump and the final base pressure of about 3.0×10^{-7} Torr is achieved with a Sumitomo Marathon CP-12 cryopump.

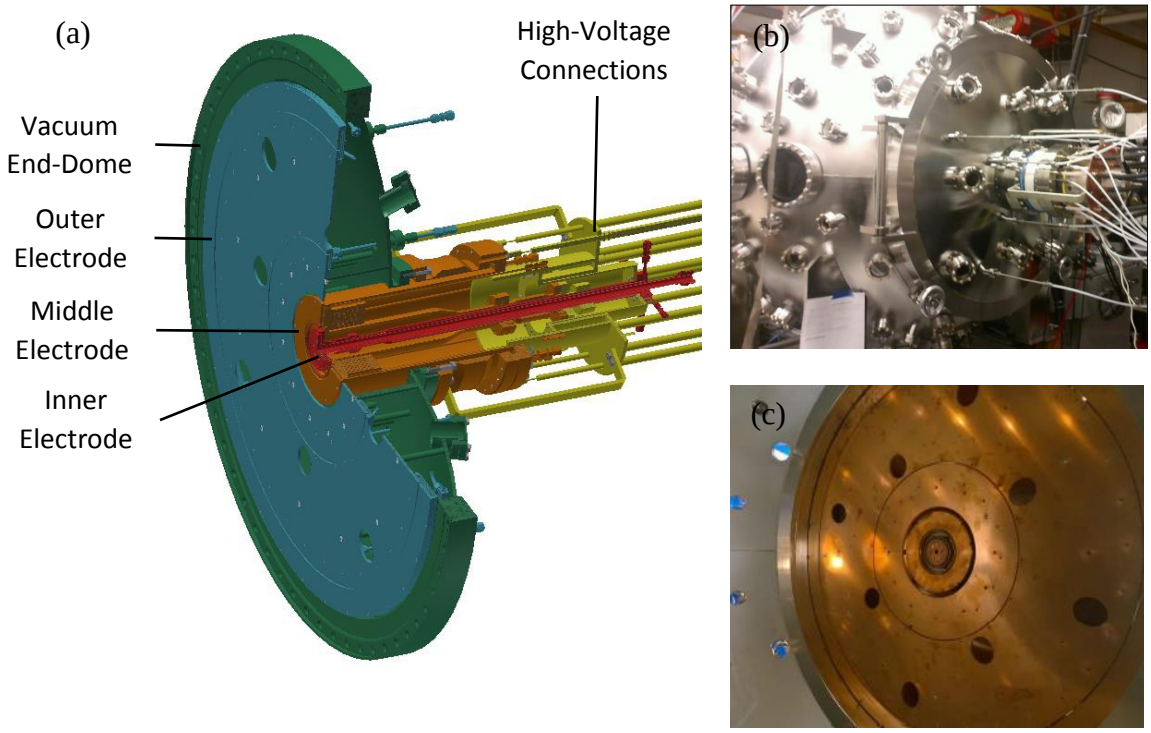

Figure 6 – The Mochi.LabJet Plasma Gun. (a) CAD drawing of Mochi.LabJet plasma gun. The gun consists of 4 assemblies mounted to the end dome (green) of a custom vacuum chamber: the inner electrode (red), the middle electrode (orange), the outer electrode (Cyan) and the high-voltage connections (yellow). (b) External view photograph of the Mochi.LabJet vacuum chamber and gun. (c) Internal view photograph of the Mochi.LabJet gun oxygen free copper electrodes.

2.1 Inner Electrode

The inner electrode assembly (Figure 7, Appendix A.2) consists of two electrically connected concentric tube sub-assemblies that terminate into two annular copper electrodes: a copper disc and cup. Neutral gas is injected through Swagelok compression tube unions at the end opposite the copper electrodes at four discrete locations. The gas then flows along the annular volume bounded by the two concentric tube sub-assemblies, and emerges through the gap between the copper disc and cup. Because the axial distance traveled by the gas is much longer than the azimuthal distance between gas injection sites, there is sufficient time for the gas to symmetrize before it reaches the copper electrodes. The inner electrode assembly is mounted to the middle electrode assembly (Section 2.2) through a high-voltage ceramic break, O-ring feedthrough and aligned with a custom made ceramic insert.

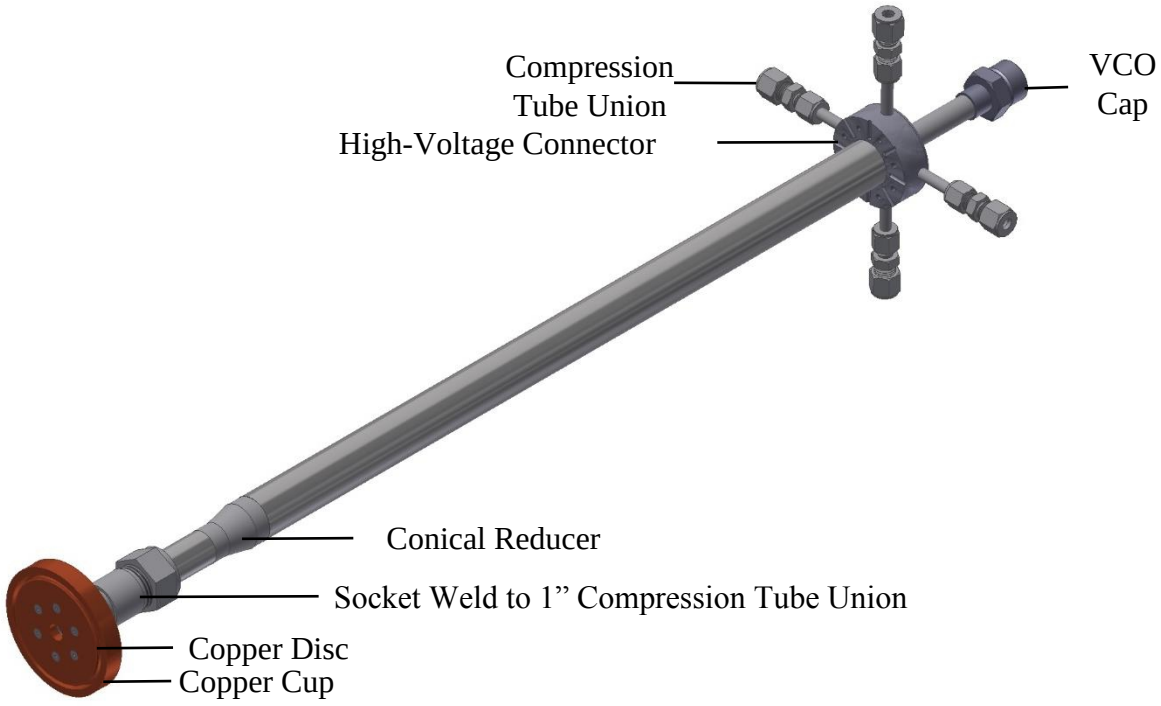

Figure 7 – Inner Electrode Assembly. The inner electrode assembly consists of two stainless steel tube assemblies terminating into two copper electrodes – a copper disc and a copper cup.

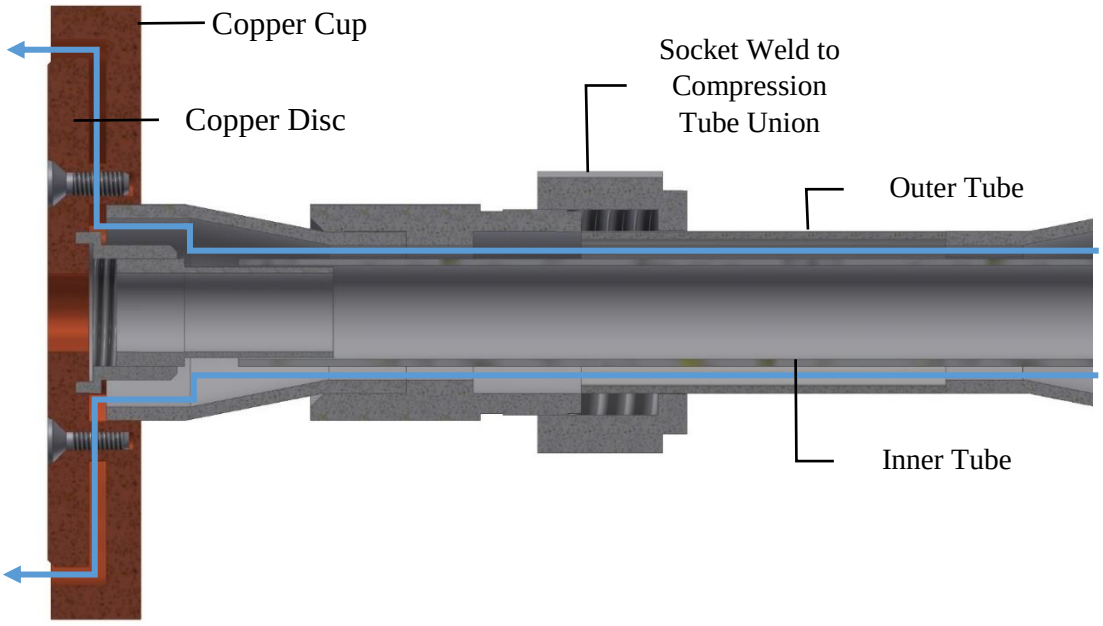

Figure 8 – Inner Electrode Gas Injection. Gas flows between the two concentric tube assemblies (blue arrows) before emerging between the gaps in the copper disc and cup. A long axial travel time should allow for sufficient azimuthal symmetry of the gas exhaust.

2.2 Middle Electrode

The middle electrode assembly (Figure 9, Appendix A.3), similar to the inner electrode assembly, consists of two electrically connected concentric tube sub-assemblies that terminate into two annular copper electrodes: an annulus and a ring. However, gas is injected through metal tubing directly to the back of the inner copper electrode. The gas then makes a small radial transit before emerging through the gap between the two electrodes. The radial distance traveled is slightly longer than the azimuthal distance between gas injection points, which will allow for symmetry of the gas exhaust. The middle electrode assembly is connected through a high-voltage ceramic break (MDC part # CE-775465003) mounted directly on the vacuum chamber. A solenoid (Section 1.2.3) that generates the background magnetic field is mounted behind the electrode, in between the two concentric tube sub-assemblies.

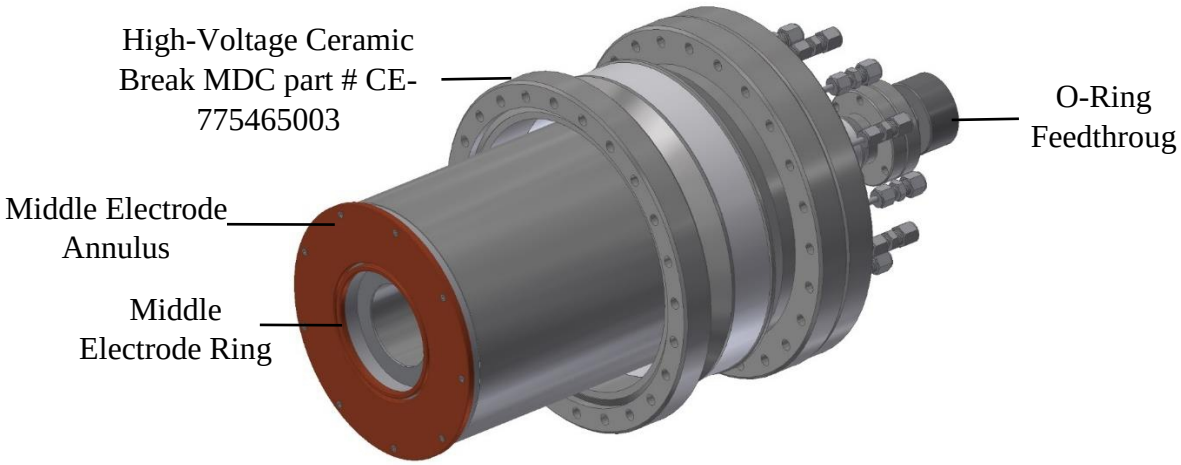

Figure 9 – The Middle Electrode Assembly. The middle electrode assembly consists of two stainless steel tube assemblies terminating into two copper electrodes – an annulus and a ring.

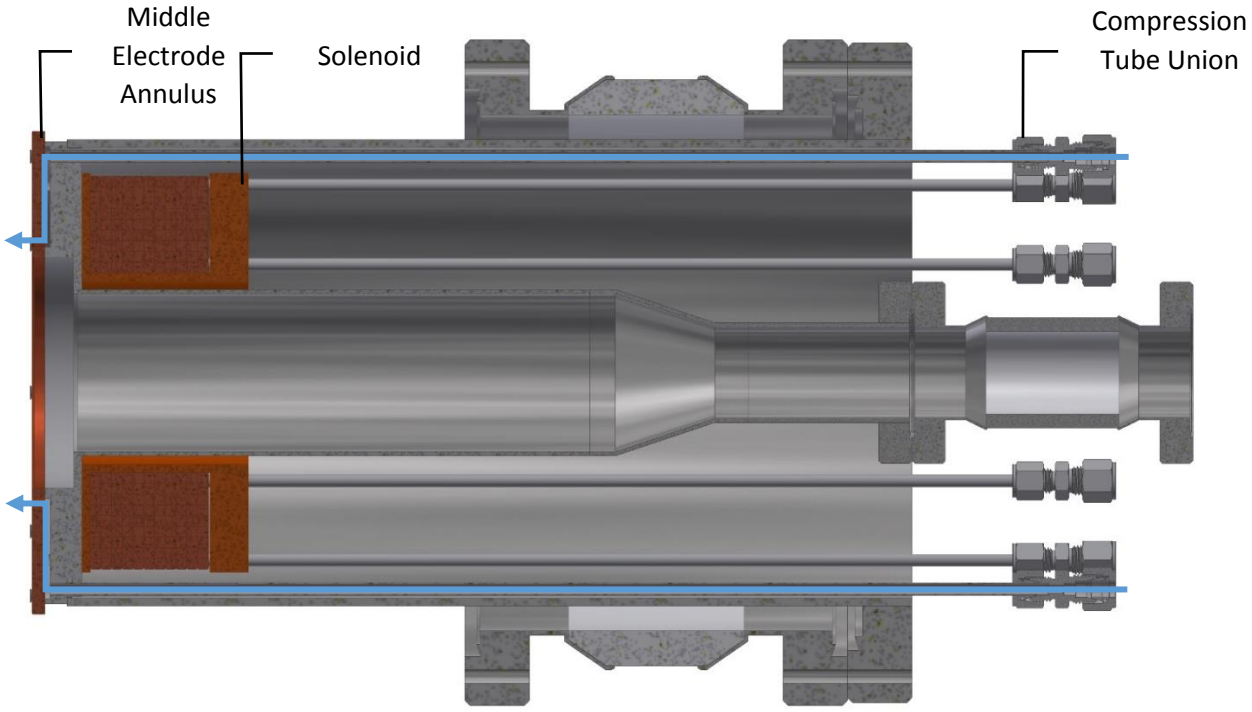

Figure 10 – Middle Electrode Gas Injection. Gas is injected into 12 stainless steel tubes that terminate behind the copper electrodes (blue arrows) and then emerge from the gap between the copper annulus and copper ring. The gas is forced into a small but appreciable radial transist, which allows for better azimuthal symmetry.

2.3 Outer Electrode

The outer electrode assembly (Figure 11, Appendix A.4), consists of three oxygen-free copper annular electrodes backed with two stainless steel gas injection plenums (Figure 11a, Appendix A.5-A.6). The entire assembly is mounted directly to the inside of the end-dome door on the vacuum chamber. For each plenum, gas is injected from custom valves into 0.25 inch metal tubing, which passes into the vacuum chamber through O-ring feed-throughs. Inside the vacuum, the tubing is split into 8 and 16 discrete gas injection locations for the inner plenum and the outer plenum, respectively. The plenums are stacked volumes that force the gas from discrete locations to travel long distances radially before emerging from the copper electrodes. Similar to the inner and middle electrode assemblies, this added travel distance allows for the gas exhaust to symmetrize. Eight cutouts allow for optical diagnostic access to the plasma.

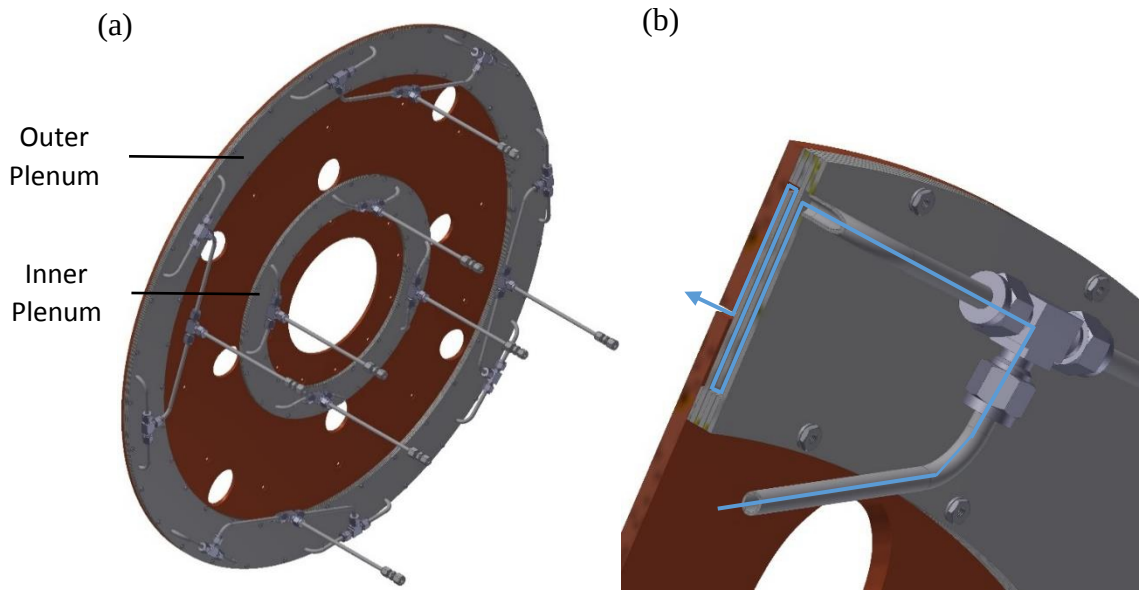

Figure 11 – Outer Electrode Assembly. (a) The outer electrode assembly consists of a copper electrode with gas injection slits backed by two gas plenums. (b) Gas is injected at discrete locations (blue arrows), and forced into long radial transists in custom plenums that have stacked volumes (Appendix A.5-A.6). The increased travel distance should provide enough time for an azimuthally symmteric gas injection to develop.

2.4 Gas Plume Model

A gas plume model was developed for determining the average Paschen criteria for plasma breakdown. The gas injected from the electrodes is modeled as closely-spaced point gas sources arranged in circles that are the dimensions of the gas slits in each electrode. Previous work [9] showed that the density of a neutral gas expanding into vacuum reduces exponentially in the axial direction and Gaussian in the $r-\theta$ plane by the following relationship:

$$n(r,z) = n_{peak}(z)e^{\left(\frac{-r}{\delta r}\right)^2} \tag{2.1}$$

$$n_{peak}(z) = n_0 e^{\frac{-z}{c}} \tag{2.2}$$

where n_0 is the source number density, r and z are the axial and radial coordinates respectively, δr is the ratio of the Mach numbers, and c is the acoustic speed. If one assumes the gas is ideal, the density is proportional to pressure following the ideal gas law and Avagadro's number

$$P(r,z) = \frac{N_{av}RTn_0 e^{\frac{-z}{c}} e^{\left(\frac{-r}{\delta r}\right)^2}}{\nu}. \tag{2.3}$$

Because the gas flow is extremely dynamic, it is unfeasible to determine n_0 analytically. Instead, this model can be fit to local measurements taken with a fast ion gauge. Figure 12 shows an $r-z$ cut plane that has been matched to fast ion gauge measurements taken at $z = 15\ cm$ above the electrodes.

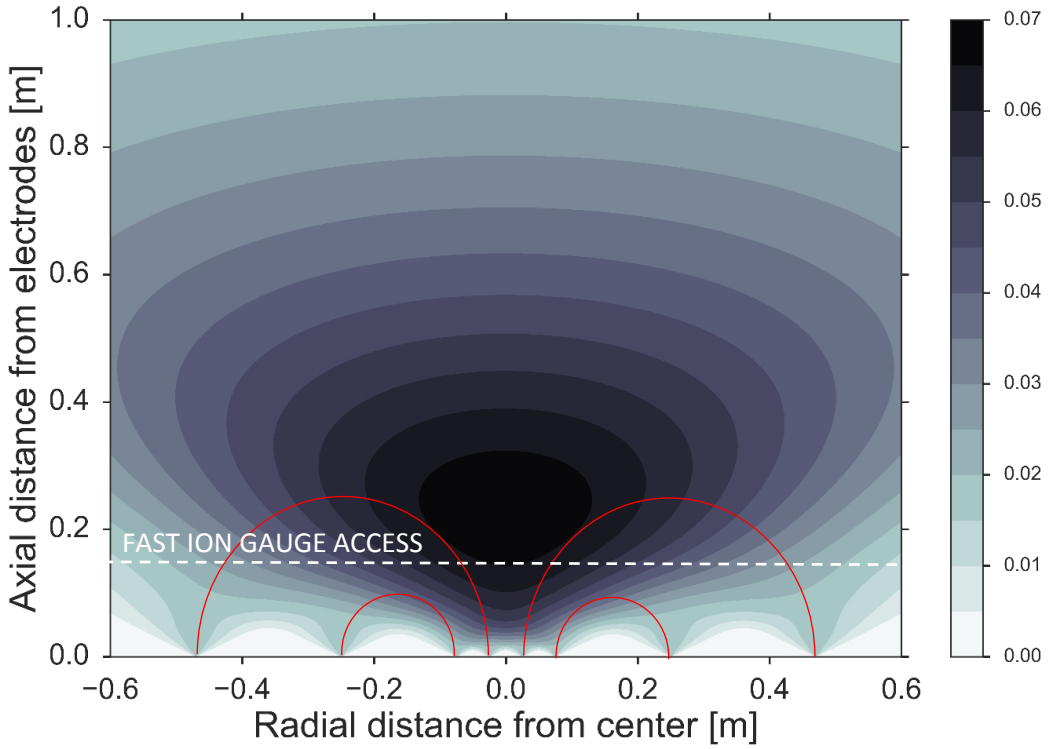

Figure 12 – Gas Plume Model. Gas slits are modeled as closely-spaced point gas sources arranged in circles with dimensions of the gas injection slits from each gun electrode assembly- pressure is in Torr. Red arcs approximate the background magnetic field linking the gas injection sites.

As expected, there are regions of high density on axis due to the close geometry of the inner and middle electrode gas injection slits, as well as regions of low density near the outer electrode gas injection slits. The pressure along the magnetic field lines is not constant. Therefore, it is difficult to determine a single pd value for Paschen's Law. Instead, a range of values is predicted. Every point along the magnetic field does not need to satisfy Paschen's Law for breakdown. Instead, breakdown is initiated at locations where Paschen's Law is satisfied, and under the appropriate conditions, breakdown will continue to propagate along the magnetic field lines.

Chapter 3 – Electrode Power Supply Units

Based on power supply design, the anticipated plasma lifetime is 10-50 μs with a total impedance of < 100 mΩ, and currents on the order of 10-100 kA. Therefore, fast, high power switches are required and connecting hardware needs to withstand potentially large stresses due to Lorentz force. Two identical, capacitor-based, ignitron-switched, optically-isolated power supply units (PSUs) were designed, built and tested for the Mochi.LabJet experiment.

3.1 High Speed Power Electronics

Typical mechanical switches, such as relays, are unsuitable for high speed and high power switching for two reasons. First, the inertia of the moving electrical conductor usually limits switching times to the ms regime. Second, although relays can have sufficient high-voltage standoff, breakdown can occur before the conductor completes contact, limiting performance and efficiency. In real circuits, semiconductor switches such as transistors, IGBTs, and SCRs, can be switched in ~100 ns [16], but are limited to moderate standoff voltages and peak currents. Triggered, gas-filled gaps such as ignitrons, thyratrons, and spark gaps can have extremely high standoff voltages, currents in excess of 100 kA, and peak power in the megawatt and gigawatt range. A summary of power switches and performance parameters are shown in Table 1 [16].

Table 1 – Switching Performance of Common Switches Used in Pulsed Power [16].

	Transistor	IGBT	SCR	Ignitron	Spark Gap
Standoff Voltage [V]	$10^1 - 10^2$	$10^2 - 10^3$	$10^2 - 10^4$	$10^4 - 10^5$	$10^4 - 10^7$
Peak Current [A]	$10^{-1} - 10^0$	$10^1 - 10^3$	$10^2 - 10^4$	$10^2 - 10^5$	$10^2 - 10^6$

The drive circuit and the physical basis for the switch are critical to the switching performance of these devices. For example, an NPN-type transistor is switched by diffusion of charge carriers, in two p-n junctions, doped at different charge concentrations. A positive potential of a few volts applied to the base-emitter junction allows for electrons to diffuse from the base to the emitter, which forces electrons in the emitter through two depletion regions of high electric fields, allowing for current to flow from the collector terminal to the emitter terminal. Typically, the ratio of current flow from collector to emitter compared to the base-emitter junction is usually 100 times greater or more. Therefore, a transistor switching 100 mA will require a driving base-emitter current of about 1 mA.

On the other hand, an ignitron is switched by generating a mercury plasma. A potential of at least a few hundred volts is applied to the ignitor with respect to the cathode terminal which causes a plasma to form from a liquid pool of mercury. The plasma quickly fills the interior of the device connecting the anode to cathode with a highly conductive fluid. Large currents are needed to sustain the plasma, which can come from the ignitor-cathode or the cathode-anode junctions. Typical ignitrons can be switched with several hundred volts at hundreds of amps, which already puts limitations on the type of switch used to drive these devices. Therefore, a series of switches scaling across power levels is usually required. For the Mochi.LabJet gun electrode power supplies, a type-D ignitron is switched by a fast ignitron trigger [17] that first switch transistors, that switch a MOSFET, that switch IGBTs, that then switch the ignitron.

3.2 Mochi.LabJet PSU2 and PSU3 Overview

Figure 13 shows the minimum component circuit diagram for each power supply which contains five General Atomics capacitors (Model 33838, 120 μF, 10 kV) connected in parallel with 1 in. wide silver plated, copper bus bar (Appendix B.2). Each capacitor bank connects directly to a custom ignitron tower (Section 3.3, Appendix B.1). Eight RG-217 coaxial cables in parallel connect each ignitron tower to the gun electrodes - PSU2 is dedicated to the middle electrode, and PSU3 is dedicated to the inner electrode. Each capacitor bank is charged with a Spellman SL300 high-voltage power supply, capable of delivering 10 kV at 30 mA. The high-voltage output from the Spellman charging supply is switched by a 'charge' Ross high-voltage relay, which is switched by the optical relay circuit (Section 3.5.3). An additional optically coupled 'dump' Ross relay connects the high-voltage terminal of the capacitors to ground through two 400 Ω silicon carbide high-power resistors, acting as a safety dump - RC discharge time constant of 240 ms. The Spellman high-voltage output is remotely adjusted using the optical tachometer circuit (Section 3.5.4) – input square pulses with frequency ~50-700 Hz corresponds to an output voltage of 1-10 kV DC.

Both power supplies are housed in wheel-mounted custom enclosures for mobility. All panels of the power supply are interlocked with a latching relay circuit. If any panel is removed while the power supply is powered, the dump relay is immediately closed to de-energize the system in about one second and the latching relay circuit must be reset to continue normal operation - acting as a fault acknowledgement system. A 3D printed control panel with switches for the charge and dump relays allow for some manual control. However, firing the power supplies is done exclusively by remote optical isolation. Each power supply is fired by triggering the ignitron through a transformer, using a fast ignitron drive circuit [17].

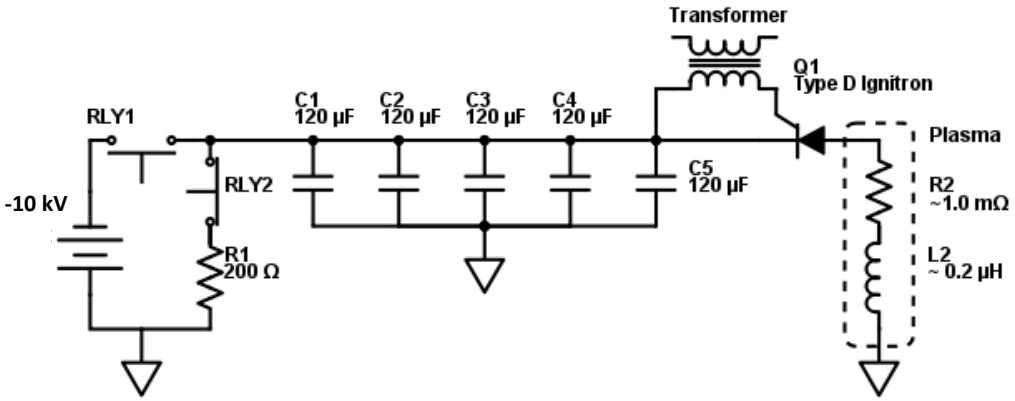

Figure 13 – Gun Electrode Power Supply Circuit Diagram.

The time required to charge the capacitors is determined by the total capacitance of the main bank and the charging current. The amount of stored charge on a capacitor is equal to the product of capacitance and voltage, $Q = CV$. Differentiating this relationship with respect to time provides a relationship for the ideal charging time of the capacitor banks, $I = CdV/dt$. The change in voltage per time for a charging current of 30 mA and a total bank capacitance of 600 μF is 50 V/s. Therefore, to charge to 10 kV requires 200 seconds, and is the limiting factor in shot repetition rate. Figure 14 shows a photograph of a complete PSU.

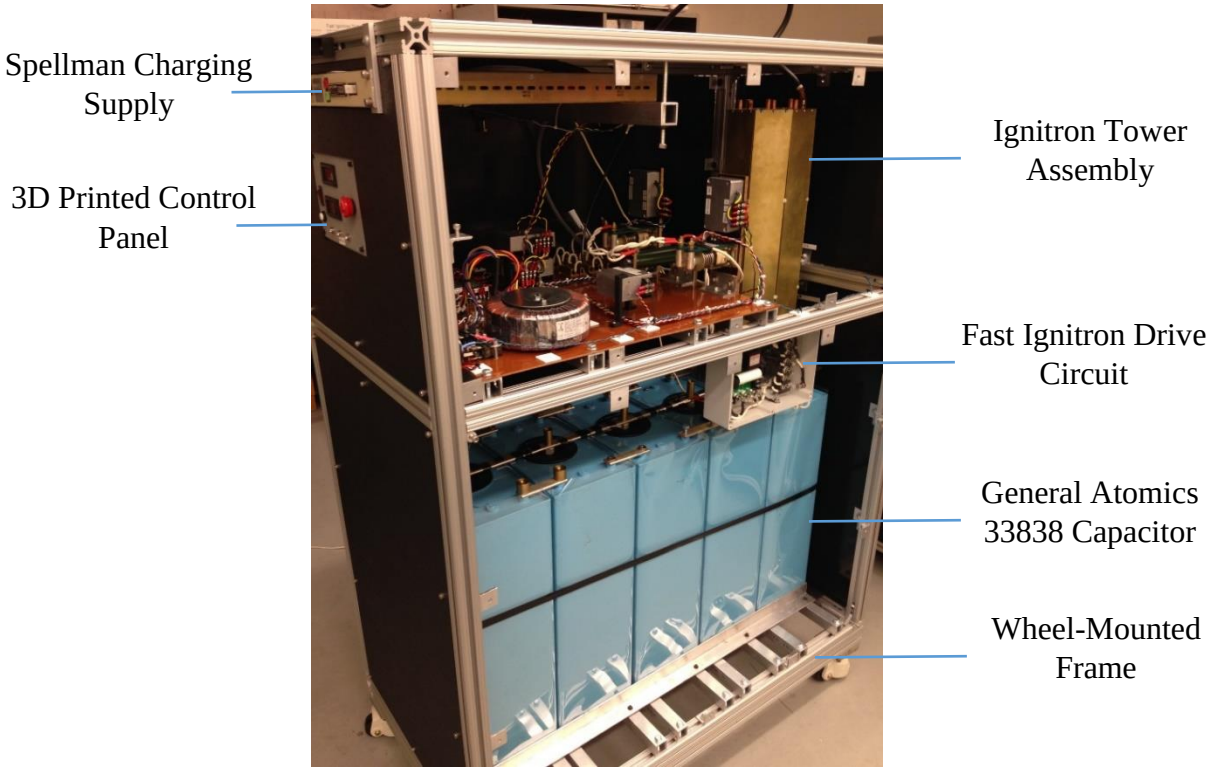

Figure 14 – Gun Electrode Power Supply Unit. (a) Photograph of finished power supply unit with enclosure panels removed to show interior components

3.3 Custom Ignitron Tower

The custom ignitron tower (Figure 15, Appendix B.1) was developed as a cost-effective and reliable high-voltage connection for a type-D ignitron which minimized inductive impedance and electromagnetic noise. The housing is made up of the forward current and return current assemblies. The forward current assembly connects the anode of the ignitron to the capacitor bank, and the cathode to the high-voltage co-axial cables which connect to the gun electrodes. As an economic alternative to a tube, the return current assembly consists of eight brass sheets that surround the forward current assembly, acting as an approximate co-axial return path. Figure 15 shows a CAD model of the high-voltage bus work and the custom ignitron tower with two brass sheets removed.

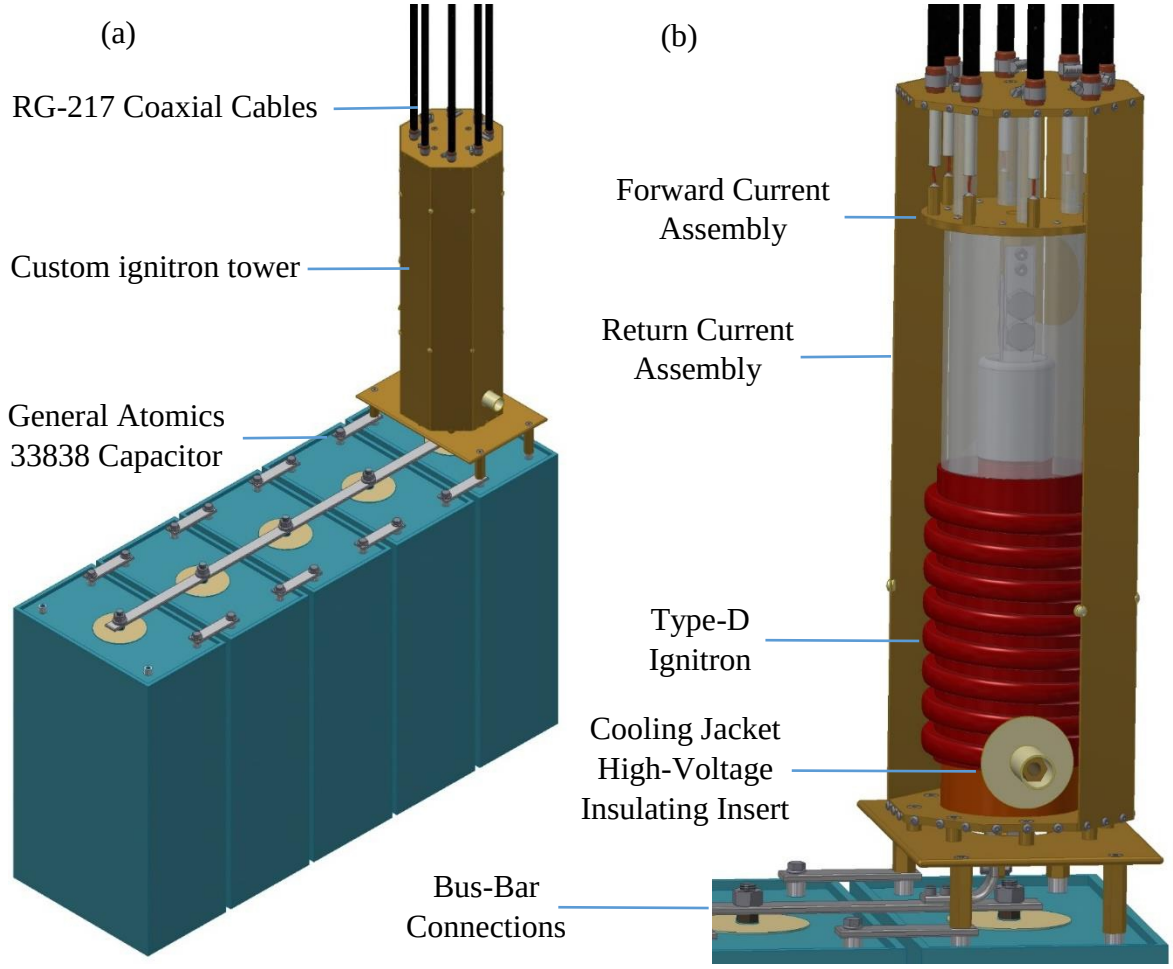

Figure 15 – Gun Electrode Power Supply Capacitor Bank and Custom Ignitron Tower. (a) CAD image of complete capacitor bank assembly, including five General Atomics 33838 120 μF 10 kV capacitors, custom ignitron tower and eight RG-217 coaxial cables. (b) CAD image of the custom ignitron tower with two return sheets removed to reveal interior components.

There are two sources that contribute to the total inductive impedance [18]: self-inductance and mutual inductance. The self-inductance of each conductor, which is a special case of mutual inductance, is determined by the geometry and where the current flows within the conductor. Typically, thin and straight will produce the least self-inductance and many simple formulas have

been derived for simple geometries [18]. The mutual inductance of a conductor is determined by the amount of flux linkages from one circuit to another. Therefore, forward and return current paths must be as close as possible to minimize the open areas of the circuit loops, while withstanding the appropriate standoff voltages. However, because there are too many circuits near and inside the power supply, the total mutual inductance cannot be determined analytically.

Additionally, the circuit is affected by the skin effect, where high frequency currents tend to flow only in the outer regions of conductors. This leads to two important design considerations. First, it is economical to reduce the cross-sectional area of conductors to the reduced area due to the skin effect, but this area needs to withstand the large electro-magnetic forces produced by the large currents. Second, because the skin effect reduces the effective cross-sectional area, the resistance is increased as a function of frequency. The current density J in a conductor due to the skin effect is defined as [19]

$$J = J_0 e^{\frac{-r}{\delta}} \tag{3.1}$$

where J_0 is the current density at the outer surface, r is the depth in the conductor, and δ

$$\delta = \sqrt{\frac{2\rho}{\omega\mu}} \sqrt{\sqrt{1 + (\rho\omega\epsilon)^2} + \rho\omega\epsilon} \tag{3.2}$$

is the skin-depth, where ρ is the resistivity, ω is the frequency of current, μ is the product of the relative magnetic permeability of the conductor and the permeability of free space, ϵ is the product of the relative permittivity of the conductor and the permittivity of free space. For Mochi.LabJet circuit parameters, the second square root quantity is approximately one and therefore the skin depth reduces to

$$\delta = \sqrt{\frac{\rho}{\mu\pi f}} \tag{3.3}$$

where f is equal to $\omega/2\pi$. For example, a copper conductor at frequencies of 10 kHz and 100 kHz (range of Mochi.LabJet experiment frequencies), produces a skin depth of 0.6 and 0.2 mm respectively.

Equation 3.3 suggests that in high frequency circuits, the resistive impedance is no longer linearly dependent on conductivity, but has a square root dependence. For example, the total resistive impedance per length for a cylindrical conductor with radius r is

$$R = \frac{\rho}{A_{effective}} = \frac{\rho}{\pi(r^2 - (r-\delta)^2)} = \frac{\rho}{\pi\left(r^2 - \left(r - \sqrt{\frac{\rho}{\mu\pi f}}\right)^2\right)}, \tag{3.4}$$

which reduces to

$$R = \frac{\rho}{\pi\left(-2r\sqrt{\frac{\rho}{\mu\pi f}} + \frac{\rho}{\mu\pi f}\right)}. \tag{3.5}$$

In the high frequency limit, where the skin effect significantly reduces the effective area, the right term in the denominator is much smaller than the left term, and the total impedance will then depend on the square root of conductivity. Comparing two materials with similar permeability, but different conductivities such as copper and austenitic stainless steel, one sees a notable effect. Copper has a conductivity about 50 times greater than stainless steel, however because of the skin depth, the effective resistance is not 50 times lower, but the square root of 50 times lower. Because of these considerations, brass, despite having a conductivity 3 times lower than copper, was chosen as an economic alternative for the custom ignitron assembly. Due to the skin effect, the total resistive impedance is only square root 3 times lower than copper and is significantly cheaper.

3.4 Circuit Simulation

A QUCS simulation was developed to estimate the performance of the power supplies. QUCS is an open source graphical circuit simulation software program [20]. Figure 18 shows the QUCS simulation for one power supply and electrode pair, which includes estimations of the inductive and resistive impedances for all of the components in the circuit, including the power supply bus work, custom ignitron assembly, transmission lines, and plasma. The estimations were performed assuming simplified geometry. For example a bus bar can be approximated as a rectangular cross-section conductor of a given length. Although, self-inductance values are tabulated for simplified geometries, it is unfeasible to calculate all of the mutual inductances in the system. Therefore, some guess work is involved and the estimation accuracy will be limited to within an order of magnitude. The correct values of all of the circuit impedances can be determined by matching the simulation to the actual experimental discharge.

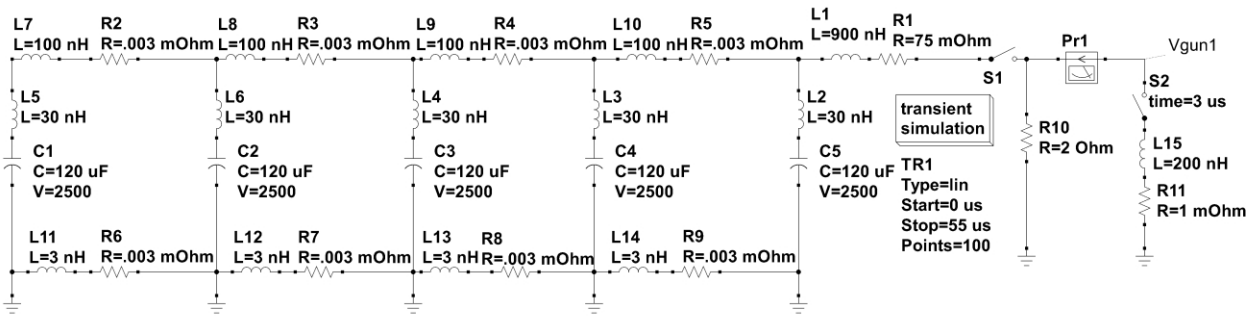

Figure 16 – PSU QUCS Circuit Simulation. QUCS simulation predicts the performance of the power supplies with the Mochi.LabJet gun. C1-C5 are the main bank capacitors, S1 represents the ignitron firing, S2 represents plasma breakdown and L15 and R11 represent the plasma inductance and resistance, repectively.

Because the plasma changes geometry and temperature as it develops, the resistive, capacitive and inductive plasma impedances are time dependent – same for the ignitron. However,

for simplicity and an initial guess, these terms are fixed in the simulation. The resistive plasma impedance can be approximated from the Spitzer resistivity η [21]

$$\eta = \frac{\pi Z e^2 m^{1/2}\, ln(\Lambda)}{(4\pi\epsilon_0)^2 (k_B T)^{3/2}} \tag{3.13}$$

which is inversely proportional to temperature and where Z is the degree of ionization, e is the fundamental charge, m is the mass of the ion species, ϵ_0 is the permittivity of free space, k_B is the Boltzman constant, and T is the temperature in electron volts. The Coulomb logarithm, $ln(\Lambda)$ is weakly dependent on plasma parameters and is assumed to be equal to 10 [21]. A singly-ionized, hydrogen plasma, with temperature ranging from 1-10 eV, yields a plasma resistance of ~1-40 mΩ.

The inductive plasma impedance can be approximated for some simplified geometries. For example, a hollow current-carrying cylinder could be an appropriate approximation for a plasma jet where most of the current density is near the edge. The inductance is a function of geometry only, and is therefore independent of other plasma parameters. The inductive impedance

$$Z_{ind} = j\omega L \tag{3.14}$$

is also a function of frequency, where ω is the angular frequency, L is the inductance and $j = \sqrt{-1}$. For a cylindrical current-carrying conductor, the self-inductance can be approximated as [18]

$$L = 0.002l\left[ln\left(\frac{2l}{\rho} - 1 + \frac{\mu}{4}\right)\right]\ [\mu H] \tag{3.15}$$

where l is the length of the conductor, ρ is the geometrical mean distance, and μ is the relative magnetic permeability, which is assumed to be 1. A plasma jet of length 30 cm and a geometrical mean distance of 5 cm will have an inductance of approximately 200 μH.

Other than the main energy storage capacitors, it was assumed that the capacitance between components was negligible, and that the circuit was dominated by inductive and resistive impedances. This assumption is justified by examining the order of magnitude of the capacitive impedance at experiment frequencies. For example, if one assumes the total inductance in the experiment is of the order $10^3\,n$H, and an experiment frequency of 10^4 Hz, the inductive impedance, from equation 3.14, is of the order $10^{-2}\,\Omega$ – similar to the expected resistive impedance. The required capacitance needed to achieve the same impedance with the same experiment frequency can be calculated from the definition of the capacitive impedance Z_{cap}

$$Z_{cap} = \frac{1}{j\omega C} = 10^{-2} \tag{3.16}$$

and solving for capacitance

$$C = \frac{1}{\omega 10^{-2}} = \frac{1}{10^4 10^{-2}} = 10^{-2}\ F \tag{3.17}$$

where C is the capacitance, ω is the circuit angular frequency and j is $\sqrt{-1}$. Because the dielectric between components is air, a capacitance of 10^{-2} would require massive surface areas, many orders of magnitude larger than what is typical of the circuit elements in the power supplies. Therefore the capacitive impedance between components is large, and does not affect the circuit. Figure 17 shows the QUCS output of plasma voltage and circuit current of the PSU circuit (Figure 16) with estimated values of resistance and inductance of each component.

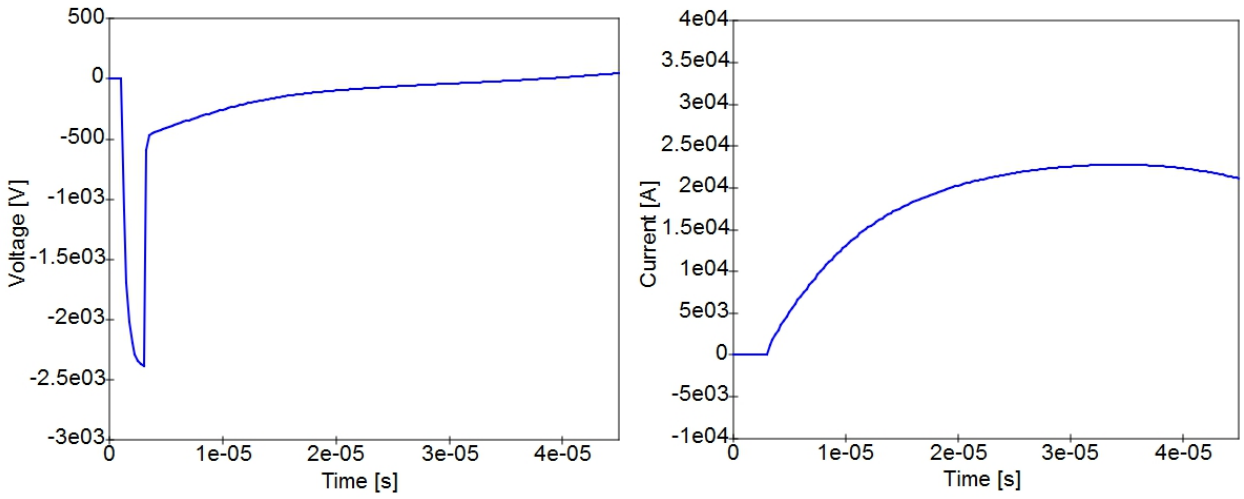

Figure 17 – Plot of PSU QUCS Simulation Output. Peak currents approach 25 kA in 30 μs, for a capacitor bank voltage of 2.5 kV.

3.5 Low Voltage Optically-Isolated Control Electronics

Each power supply requires six different user inputs for complete operation: toggle charge Ross relay (120 VAC 60 Hz), toggle dump Ross relay (120 VAC 60 Hz), set charging voltage (1-10 VDC), disable Spellman internal interlocks (short-circuit), enable Spellman high-voltage out (short-circuit), and fire the PSU (optical pulse). A typical control sequence for a single plasma shot is as follows:

1. Toggle dump relay open
2. Set charging voltage
3. Disable Spellman internal interlock
4. Enable high-voltage out
5. Toggle charge relay closed
6. Charge capacitors
7. Toggle charge relay open

8. Fire
9. Dump relay closed
10. Disable high voltage out
11. Enable Spellman internal interlock

Manually toggling the Ross relays requires switching 120 VAC, which is accomplished through a rocker switch on the front panel. For optically-isolated remote operation, the 120 VAC is switched by a reed relay in the optical relay circuit. Setting the charging voltage under manual operation, requires using the voltage adjust on the Spellman's front panel. For optically-isolated remote operation the Spellman power supply requires a DC input voltage of 1-10 V, which is accomplished through the optical tachometer circuit. Manually disabling the internal interlocks and enabling high-voltage out is achieved through switches on the Spellman's front panel. For optically-isolated remote operation, this is achieved with two optical relay circuits. Firing the power supply is done exclusively with remote optical isolation using the fast ignitron trigger circuit [17].

3.5.1 TTL-Optical Transmitter Circuit

A low voltage TTL signal is first generated through a single channel of a National Instruments timing card, and triggers the base terminal of a NPN transistor (Q1) in a custom transmitter circuit (Figure 18). When the base of the transistor is high, current from the emitter drives an 820 nm wavelength AlGaAs LED in a commercial optical transmitter (Avago Technologies HFBR-1214TZ). The red light from the transmitter then propagates through a glass fiber-optic chord to each of the power supplies. The optical signal is then converted back to low

voltage TTL signals through the optical-TTL receiver circuit (Section 3.5.2), optical relay (Section 3.5.3), optical tachometer (3.5.4) or the fast ignitron trigger [17] circuits.

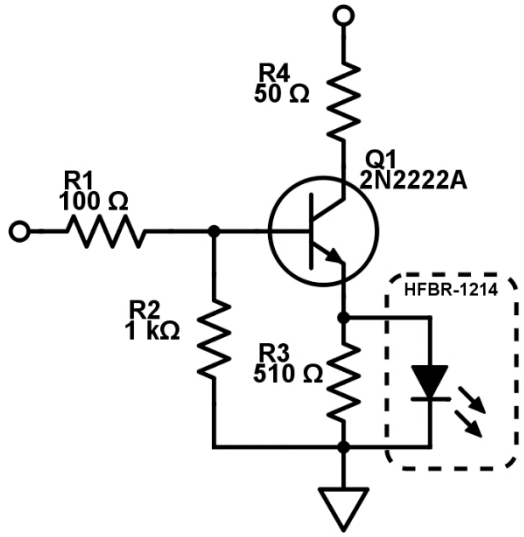

Figure 18 – TTL-Optical Transmitter Circuit. Converts TTL voltage signals generated from National Instruments timing cards PXI-6602/6132 to optical signals that are used to control the power supplies. This custom circuit uses 25% of the power of traditional circuits for driving the HFBR-1214 commercial optical transmitter.

3.5.2 Optical-TTL Receiver Circuit

Figure 19 shows the circuit for the optical-TTL receiver circuit. A commercial optical receiver (Avago Technologies HFBR-2412TZ), which includes an integrated photodetector, DC amplifier, and Shottkey-clamped transistor, receives the optical signals sent from the TTL-optical transmitter circuit and triggers the nominally high base terminal of the first NPN transistor (Q1) in a pair by shorting it to ground. The base terminal of the second transistor (Q2) is connected to the collector of the first (Q2). Thus, if the first transistor's (Q1) base terminal is low and the second's (Q2) is high, current can flow from the second transmitter's (Q2) emitter terminal. A Baker's

clamp, which consists of three diodes (D1, D2, D3), allows faster shutoff times on the first transistor (Q1), which allows for faster turn-on times for the second (Q2).

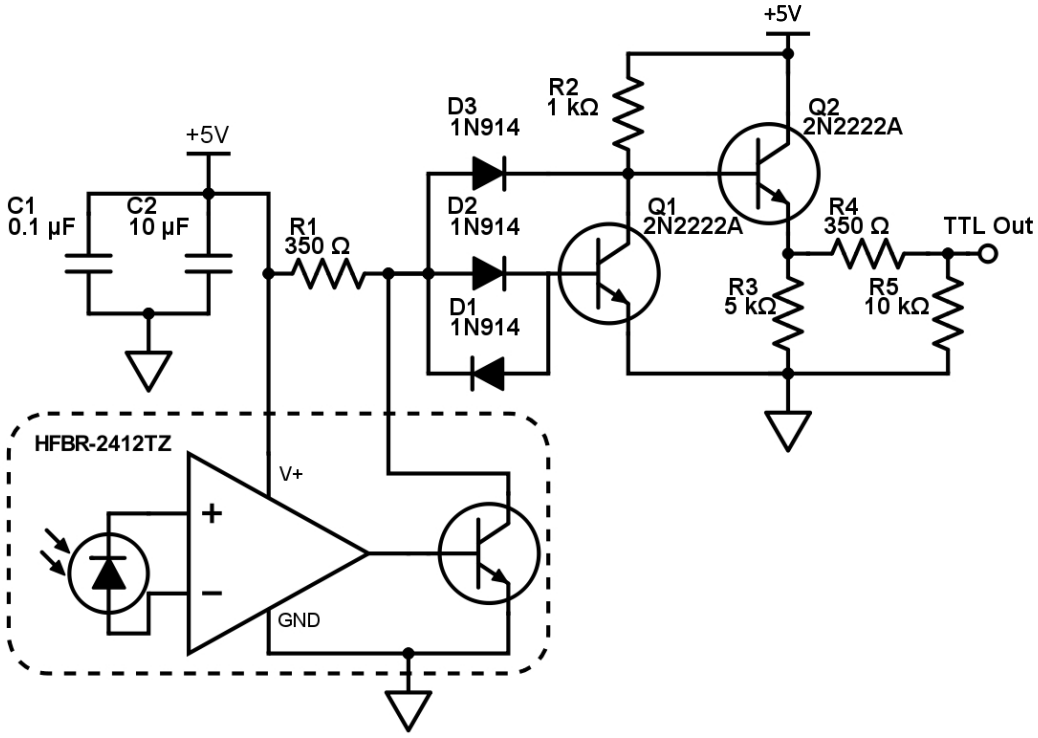

Figure 19- Optical-TTL Receiver Circuit. Converts optical signals sent from the optical transmitter circuit back to TTL voltage signals and is an integral part of the optical relay and optical tachometer circuits.

Figure 20 shows a plot of the typical performance of the optical TTL circuit. A 15 μs TTL pulse is generated from the NI timing cards (PXI-6602/6132) and a custom LabVIEW VI. The TTL pulse is converted to a light pulse using the TTL-optical transmitter circuit (Figure 18) and propagates on 30 meters of fiber-optic chord. The light pulse is then converted back to a TTL signal in a total delay of 281 ns (Figure 20b). The shutoff time is around a few μs.

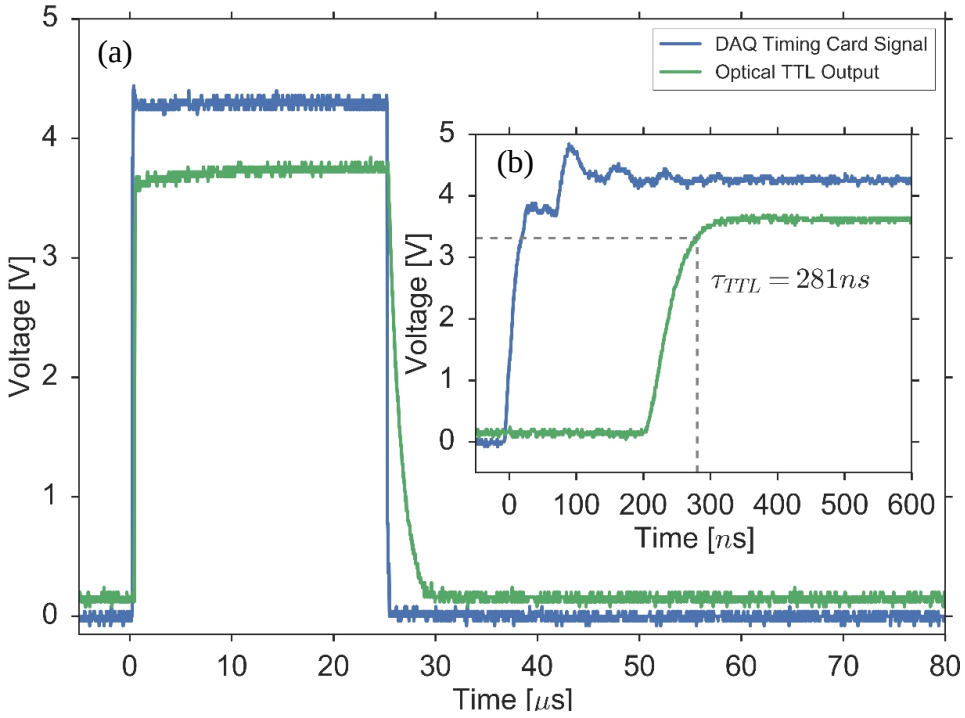

Figure 20 – Optical-TTL Receiver Circuit Switching Times. (a) A 25 μs long TTL voltage signal (blue) is generated from a National Instruments timing card, converted to an optical signal through the TTL-optical transmitter circuit, propagates on 30 meters of fiber-optic chord and converted back to a TTL voltage signal (green). Shut off times are a few microseconds. (b) Total delay τ_{TTL} to 90% rise of the optical to TTL signal is 281 ns.

3.5.3 Optical-Relay Circuit

The optical-relay circuit (Figure 21) contains the optical-TTL receiver circuit and includes a MOSFET (IRF540), but excludes a Baker's clamp. Because the relay is a mechanical switch and its inertia dominates the switching times (10-100 ms), the Baker's clamp is not needed. The MOSFET (Q3), triggered by the second transistor (Q2), drives a 12 VDC reed relay that is used to drive higher power components, such as Ross high-voltage relays. The reed relay also separates high power from the low power circuitry. Figure 22 plots the typical performance of the optical-relay circuit. A 25 ms TTL signal is generated from the NI timing cards and is converted to an

optical signal using the TTL-optical transmitter circuit. The signal is then converted back to a TTL signal that triggers a MOSFET in about 615 ns (Figure 22b). However, because of the inertia of the contacts, the relay is switched in about 15 ms. The signal oscillates (Figure 22a - red curve at ~15 ms) because the conductors of the reed relay are bouncing and vibrating when first switched, leading to poor contact.

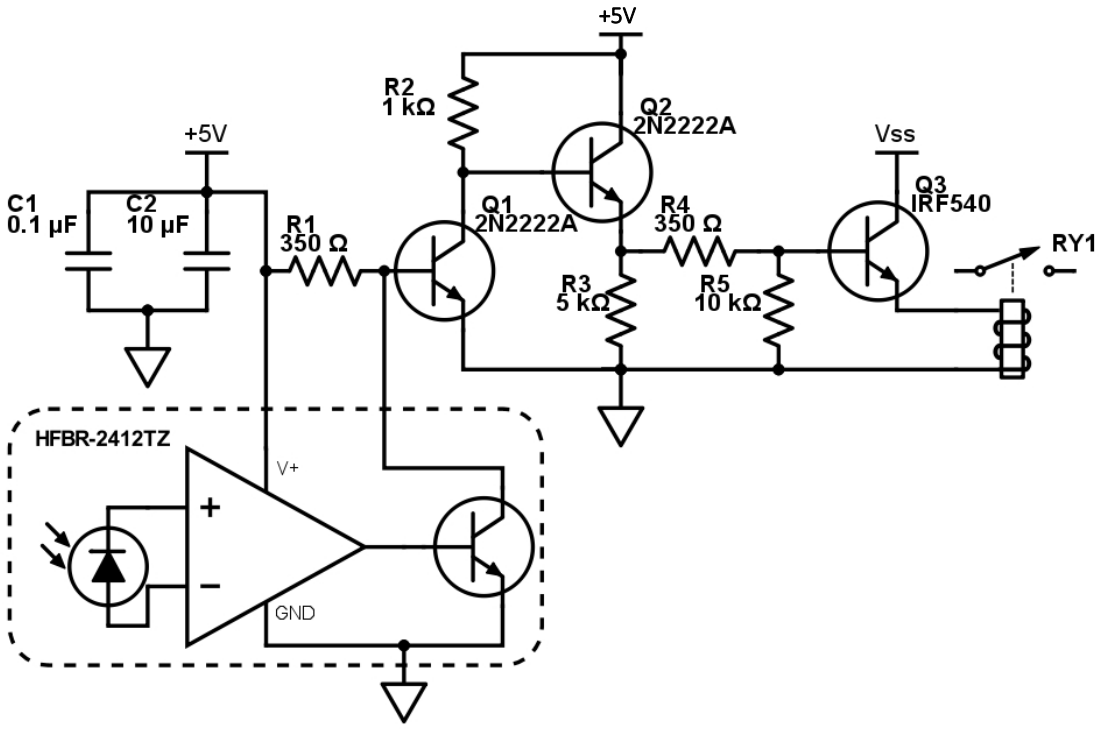

Figure 21 – Optical-Relay Circuit. Converts optical signals to TTL voltage signals that are used to trigger a MOSFET. The MOSFET can then be used to drive higher power components such as a reed relay or SCR.

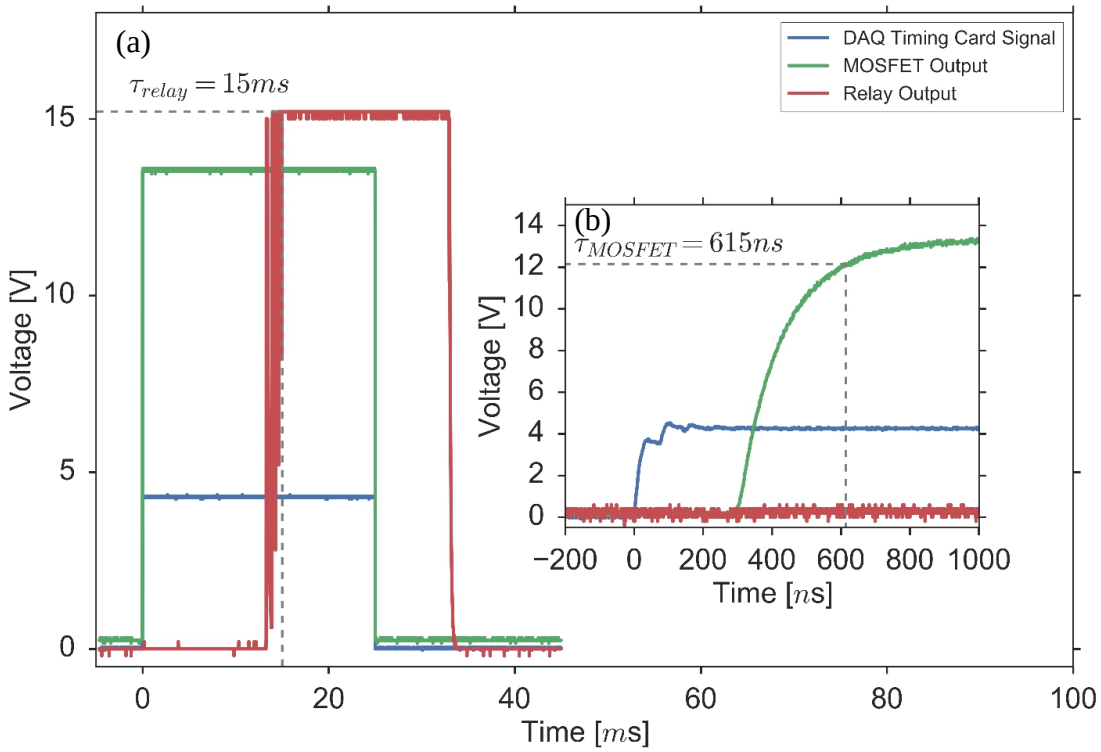

Figure 22 – Optical-Relay Switching Times. (a) A 25 ms long TTL voltage signal (blue) is generated from a National Instruments timing card, converted to an optical signal through the TTL-optical transmitter circuit, propagates on 30 meters of fiber optic chord to the optical-relay circuit and triggers a MOSFET (green) which drives a reed relay (red). The reed relay's contact inertia limits the switch time τ_{relay} to 15 ms and causes significant jitter. (b) The MOSFET switch time τ_{MOSFET} is 615 ns.

3.5.4 Optical-Tachometer Circuit

The optical-tachometer circuit (Figure 23), uses the optical-TTL receiver circuit and the recommended drive circuit for a digital-to-analog converter (Texas Instruments IC LM2907). TTL pulses at a specified frequency are set in LabVIEW, and converted to optical signals by the TTL-optical transmitter circuit. These optical signals are received by the optical-TTL receiver circuit, which are then converted to TTL voltage pulses that are fed to pin 1 on the LM2907. The LM2907 counts crossings with respect to pin 11, which is biased using a voltage divide. The number of

counts in time is proportional to a DC output voltage that can be used to control components, such as the charging voltage of a power supply.

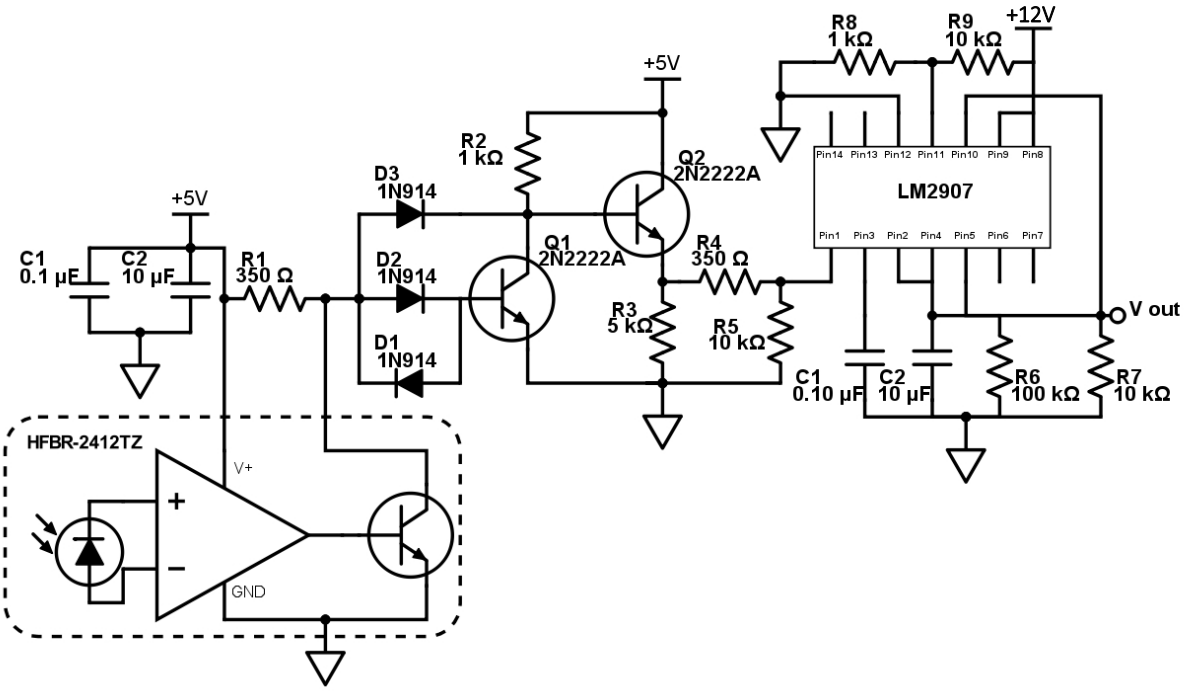

Figure 23 – Optical-Tachometer Circuit. The optical-tachometer circuit converts optical pulses of a given frequency to analog DC voltages. Input square pulses will produce DC output voltages that are linearly dependent on the pulse frequency.

Figure 24 plots a typical output of the optical-tachometer circuit (Figure 23) with an input frequency of 274 Hz, producing a continuous output of 4 VDC. During operation, the user selects a desired voltage and a LabVIEW VI interpolates the value from a calibration curve (Figure 24b), and the National Instruments timing cards output square pulses of the desired frequency. The optical-tachometer circuit receives these square pulses and sends the Spellman charging supplies a DC input voltage of 1-10 V which corresponds to an output voltage of 1-10 kVDC. The entire setup thus enables full, optically-isolated, remote control of the gun electrode power supplies – for safety and convenience.

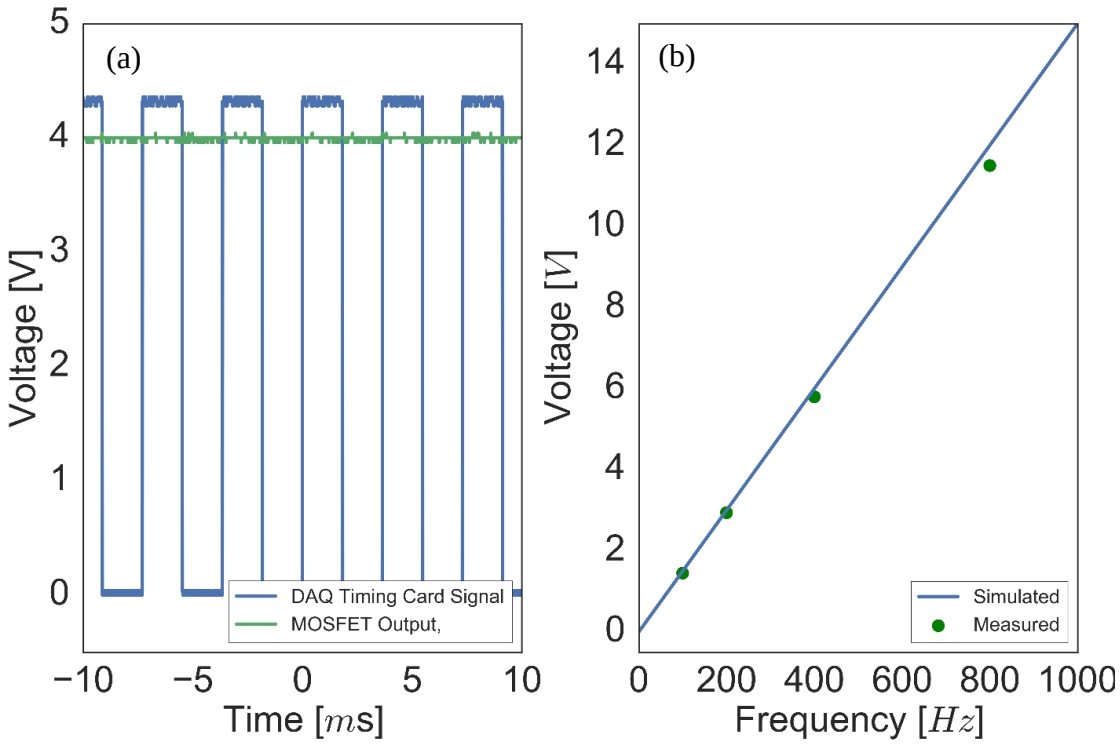

Figure 24 – Optical-Tachometer Circuit Performance. (a) The optical-tachometer circuit outputs a continuous 4 VDC by inputting optical pulses with a frequency of 274 Hz. (b) The optical-tachometer circuit is linearly dependent on the frequency of the input optical pulses. The calculated voltage vs. frequency found in the data sheet is plotted against measured values of a real circuit.

Chapter 4 – First Plasmas

At present, in the midst of the commissioning phase of the apparatus, the Mochi.LabJet experiment has operated with the middle and outer electrode pair only.

4.1 Flared Plasma Jet

Figure 25 and 26 show voltage and current traces of shot numbers 3080-3091 that show evidence of flared jet structures (Figure 27) in fast-framing camera images. The neutral gas species is diatomic hydrogen and the middle electrode potential is -2.5 kV with respect to the outer electrode. The middle and inner plenum gas timings are -3 and -5 ms respectively.

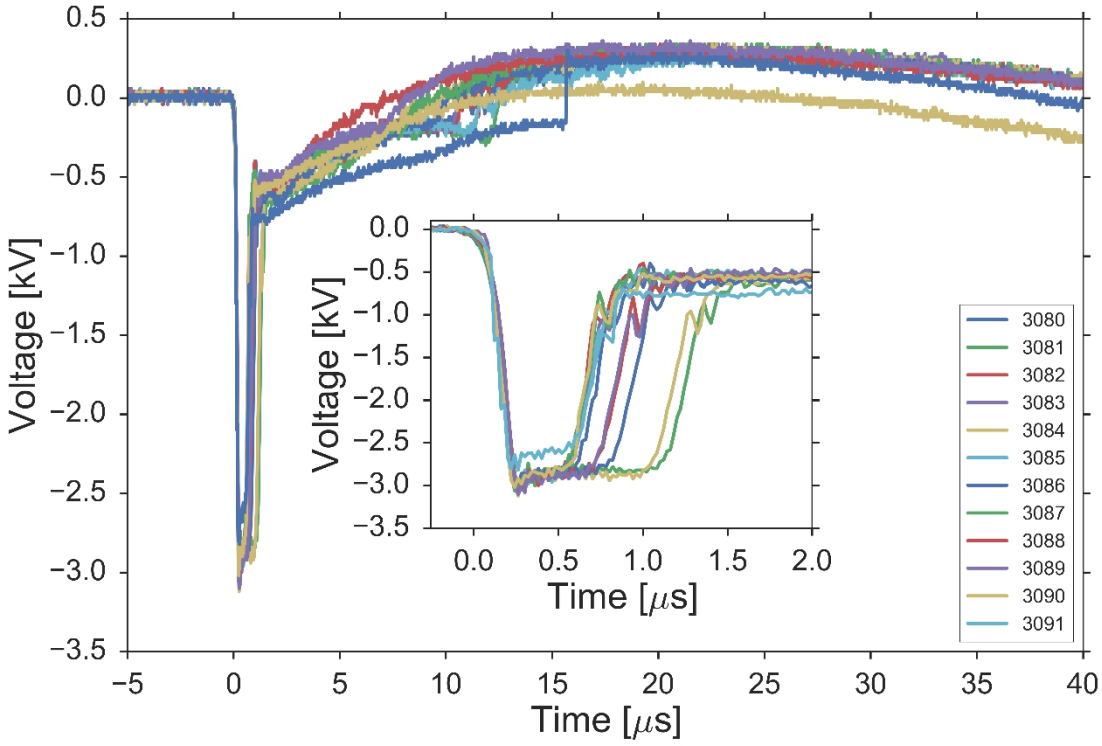

Figure 25 – Votlage Traces for Shots 3080-3091. Chosen because camera images show evidence of flared jet (Figure 27).

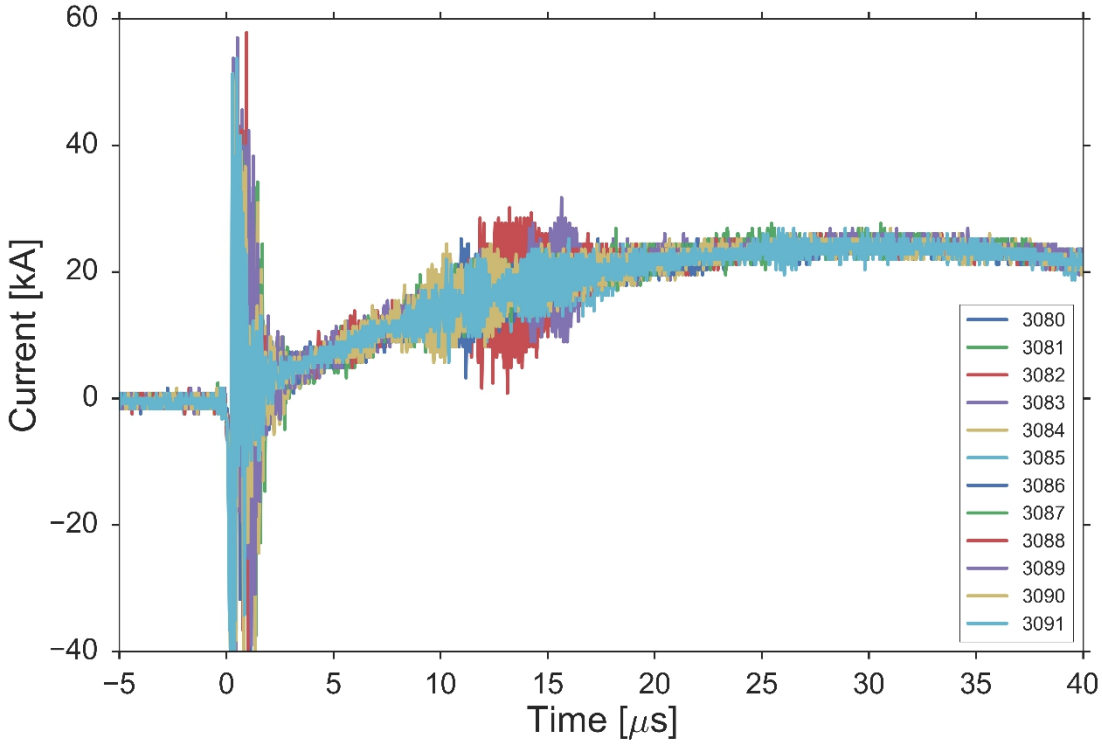

Figure 26 - Current Traces for Shots 3080-3091. Chosen because camera images show evidence of flared jet (Figure 27).

For each shot, at $t = 0$, PSU2 is fired, and the middle electrode potential quickly falls to around -2.5 kV. In ~1-2 microseconds, breakdown occurs and the voltage quickly increases to about -500 V, which is determined by the ratio of the time-dependent plasma impedance to the impedances of the other circuit elements including: the transmission lines, ignitron assembly, etc. The peak current lags the peak voltage by approximately 10 μs, as expected for a inductively dominated circuit. Peak currents approach 25 kA in about 25 μs. The peak instantaneous power dissipated through the plasma is a few megawatts.

Figure 27 depicts the time evolution of the middle electrode plasma for shots 3080-3091 Breakdown is initiated with a single arch of plasma that develops into multiple arches, and an

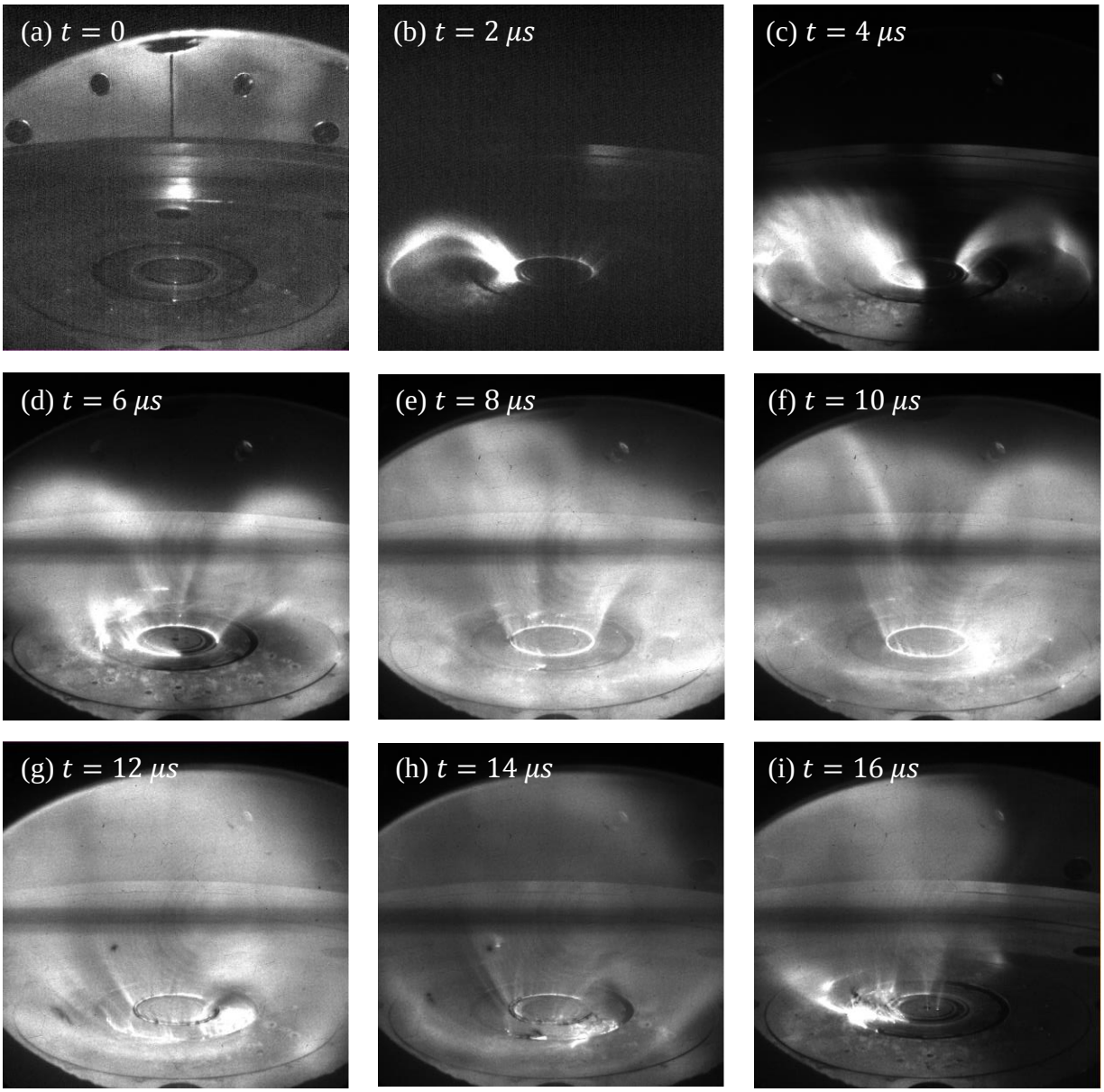

Figure 27 - Time Evolution of Flared Plasma Jet. Constructed from shots 3080-3091 by stepping camera acquisition times by 2 μs. (a) Background image before plasma breakdown. (b) A single arch of plasma initiates breakdown. (c) Multiple arches develop. (d) Plasma arches start to flare. (e) Complete azimuthal breakdown and fully developed flared jet. (f) The flared jet collimates slightly. (g)-(i) Breakdown occurs in gap between electrodes possibly disrupting plasma development.

azimuthally complete breakdown resembling the Bundt cake tin (Figure 1b). The inner region of the Bundt cake formation pinches towards the axis due to electromagnetic forces, while the outer region expands creating a flared plasma jet. The Bundt cake formation occurs approximately from

2 to 8 μs and current starts to ramp up. A fully-developed, flared plasma jet seems to occur just as the voltage crosses zero and becomes positive. Despite observation of flared jet structures generated from the two electrodes of the Mochi.LabJet experiment, these preliminary plasmas do not show strong collimation as observed on the Caltech experiment in Figure 3.

Figure 28 shows a current comparison of shot 3085 and the QUCS Simulation from section 3.4 (Figure 16). Despite the QUCS model having time independent approximations for the plasma and ignitron impedances, the shape and amplitude of the currents approximately match.

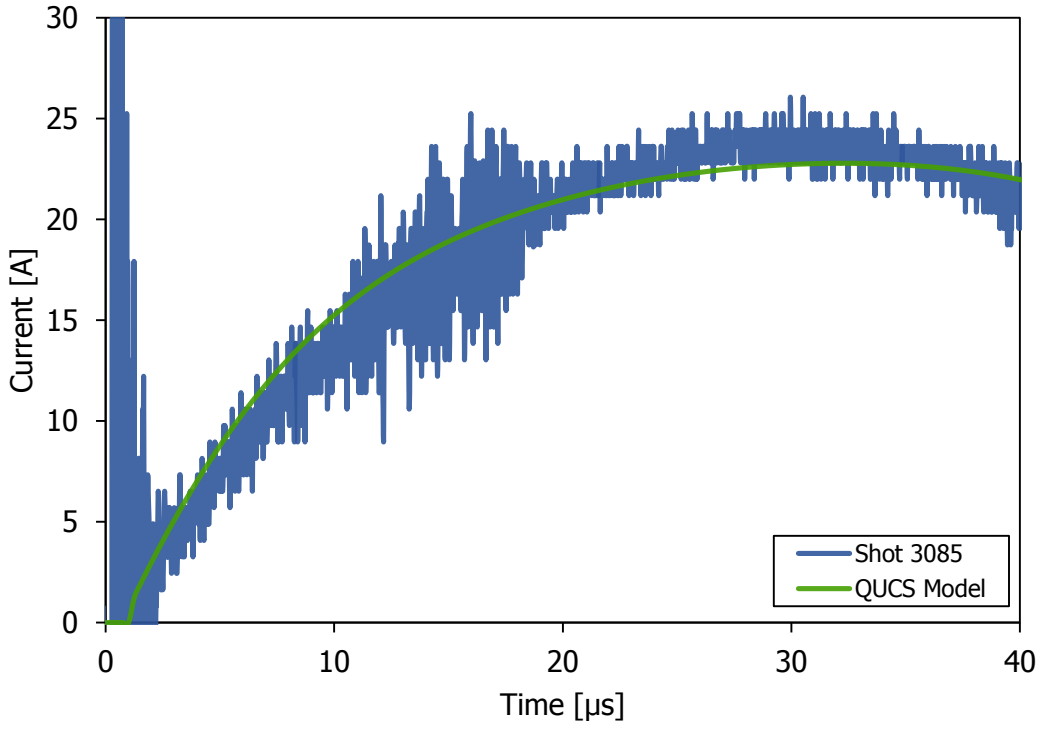

Figure 28 – Current Comparison of Shot 3085 with QUCS Simulation (Figure 16). The plasma inductance and resistance is approximated as 200 nH and 1 mΩ, respectively.

4.2 The Bundt Cake Formation

Figure 27 shows strong asymmetry in the initial breakdown which could be a result of poor gas injection symmetry. However, exploring different gas timings and electrode potentials, has shown strong evidence of symmetrical gas injection which suggests that the asymmetry is most likely due to relative timings of gas injection or type of gas valve used. For example, Figure 29a shows an image of shot 3319 which displays a clear Bundt cake formation. The neutral gas species is diatomic hydrogen and the middle electrode potential is -2.5 kV with respect to the outer electrode. However, two commercial high speed vacuum dispensing Parker valves (Series 99) are used for the inner plenum instead of the Mochi.Labjet custom fast-gas valves. The gas timings are -4 ms and -5 ms for the Parker valves and the custom valve respectively. The strength of the bias magnetic field was not changed.

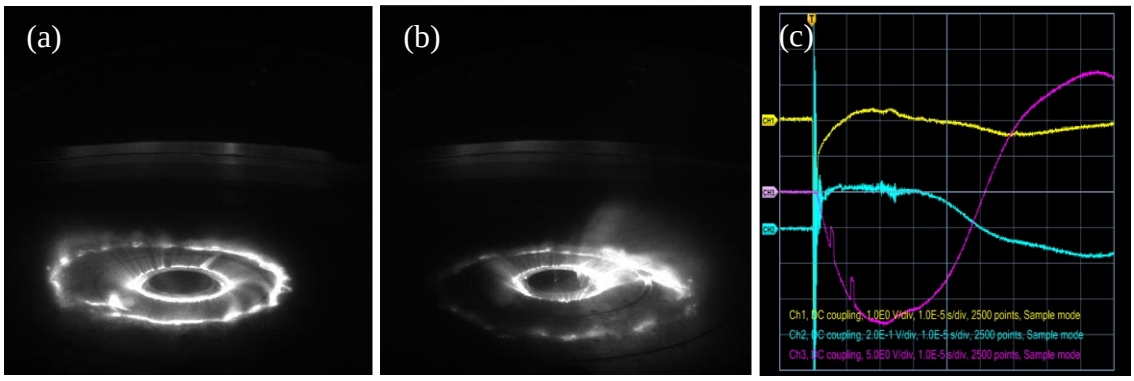

Figure 29 – Bundt Cake Formation. (a) Strong evidence of an azimuthally symmetric Bundt cake formation (shot # 3319). (b) Bundt cake formation still occurs without outer-inner gas injection (shot #3323). (c) Uncalibrated Rogowski coil trace shows flat current profile (cyan).

There are three interesting features of this regime and equipment configuration. First, the Bundt cake structure readily forms and shows appreciable symmetry (Figure 29a); however, a flared jet does not develop later in time. Second, the inner arches from the Bundt cake seem to align with the middle electrode gas injection site, but terminate into a region of the outer electrode

where there should be no gas. Upon further investigation, it is evident that most of the gas fueling is from the middle electrode and the custom valve. This is readily verified by not firing the Parker valves that inject gas into the inner plenum during a shot and still imaging a similar plasma structure (Figure 29b). Third the current traces (Figure 29c) exhibit flat profiles, which suggest that the power supplies and plasma could already behave as a pulse-forming network. A flat current profile of approximately 20 kA persists for nearly 40 μs.

Chapter 5 – Conclusion

This thesis details the development of the Mochi.LabJet experiment, designed to investigate the interaction of flows in laboratory plasma jets relevant to astrophysical jets launched from accretion disc systems. The experiment requires three pulsed-power supplies and a three electrode coplanar coaxial plasma gun with azimuthal symmetric gas injection - mounted to a 1.4 meter spherical vacuum chamber.

Chapter 2 discusses the design of a three electrode, coplanar and coaxial, magnetized plasma gun with azimuthal symmetric gas injection. The gun consists of 4 separate assemblies: inner electrode, middle electrode, outer electrode and high-voltage connections. All three electrode assemblies force injected gas into long radial or axial transits, allowing for azimuthally symmetric exhaust plumes to develop. Once the gas emerges from slits in the electrodes and expands into vacuum, the density decreases exponentially and Gaussian in the axial and radial directions respectively. The breakdown characteristics of the gun are determined from this non-uniform gas expansion and application of Paschen's Law.

Chapter 3 discusses the design of two identical, capacitor-based, ignitron-switched, and optically-isolated, pulsed-power supplies. DC operation is unfeasible because high-voltage and large currents are required for plasma generation and sustainment, with powers on the order of the megawatt. Each power supply can produce voltages and currents up to 10 kV and 100 kA respectively for plasmas with time scales on the order of 10-50 μs. A custom ignitron tower was developed as a low cost, low impedance housing for connecting a type D ignitron to the rest of the circuit. For safety and convenience, the power supplies can be operated remotely with complete optical isolation. Four custom circuits are required to optically toggle relays, set

charging voltage and fire the experiment: the TTL-optical transmitter, optical-TTL receiver, optical relay and optical tachometer circuit.

Chapter 4 discusses the first plasmas during the commissioning phase of the Mochi.LabJet experiment with operating only the middle and outer electrode pair. Presently, the Mochi.LabJet experiment has observed evidence of flared jet structures and Bundt cake formations with fast-framing camera images; however, without the strong collimation observed on the Caltech experiment. Peak currents approach 25 kA in 25 μs, for a power supply bank voltage of -2.5 kV. A flat current profile of 20 kA lasting 40 μs was observed which suggests that the circuit may already behave as a pulse-forming network. Commercial gas valves, such as the Parker Series 99, have insufficient opening times and gas throughput for the Mochi.LabJet experiment. Experimental discharges match amplitude and shape of currents predicted by QUCS model.

The next steps in the commissioning phase include operating with both electrode pairs simultaneously, and fully exploring the Mochi.LabJet experiment's parameter space. The second electrode pair will allow for the possibility of strong shear flows. Additional diagnostics, presently under construction, are required for measurements of temperature, density, magnetic field, jet current profile, and local jet flow velocities.

Bibliography

[1] P. Hartigan, S. Heathcote, J.A. Morse, B. Reipurth, and J. Bally. "Proper motions of the HH 47 jet observed with the Hubble Space Telescope." *The Astronomical Journal* 130.5 (2005).

[2] K. Asada, M. Inoue, Y. Uchida, S. Kameno, K. Fujisawa, S. Iguchi, and M. Mutoh. "A Helical Magnetic Field in the Jet of 3C 273." *Publ. Astron. Soc. Japan*. 54.3 (2002).

[3] R.V.E. Lovelace. "Dynamo Model of Double Radio Sources." *Nature* 262 (1976).

[4] P.M. Bellan. *Fundamentals of Plasma Physics.* New York: Cambridge University Press 2008.

[5] D.D. Ryutov, R.P. Drake and B.A. Remington. "Criteria for Scaled Laboratory Simulations of Astrophysical MHD Phenomena." *The Astrophysical Journal* 127.2 (2000).

[6] F. Suzuki-Vidal, S. V. Lebenev, A. Ciardi, S. N. Bland, J. P. Chittenden, G. N. Hall, A. Harvey-Thompson, A. Marocchino, C. Ning et al. "Formation of Epidsodic Magnetically Driven Radiatively Cooled Plasma Jets in the Laboratory." *Astrophysics and Space Science* 322.1 (2009).

[7] S. C. Hsu and P. M. Bellan. "A Laboratory Plasma Experiment for Studying Magnetic Dynamics of Accretion Discs and Jets." *Mon. Not. Royal Astron. Soc*. 334 (2002).

[8] R.J. Goldston and P.H. Rutherford. *Introduction to Plasma Physics*. Boca Raton: CRC Press 1995.

[9] S. You, G. S. Yun, and P. M. Bellan. "Dynamic and Stagnation Plasma Flow Leading to Magneitc-Flux-Tube Collimation." *Physical Review Letters* 95.4 (2005).

[10] P. M. Bellan. "Why Current-Carrying Magnetic Flux Tubes Gobble Up Plasma and Become Thin as a Result." *Physics of Plasmas* 10.5 (2003).

[11] G. Bateman. *MHD Instabilities*. Cambridge: The MIT Press, 1978.

[12] S. C. Hsu and P. M. Bellan. "On the Jets, Kinks and Spheromaks Formed by a Planar Magnetized Coaxial Gun." *Physics of Plasmas* 12 (2005).

[13] U. Shumlak, B. Nelson, R. Golingo, S. Jackson, E. Crawford and D. Den Hartog. "Shear Flow Stabilization Experiments in the ZaP Flow Z-Pinch." *Physics of Plasmas* 10.5 (2003).

[14] P.M. Bellan. "Thermal Instability of Electrolytic Capacitor Bank Used For Gas Puff Valve." *Review of Scientific Instruments* 73.8 (2002).

[15] P.M. Bellan. *Spheromaks*. London: Imperial College Press, 2000.

[16] S.T. Pai and Q. Zhang. *Introduction to High Power Pulse Technology*. London: World Scientific Publishing Co., 2003.

[17] V. Chaplin and P.M. Bellan. "Fast Ignitron Trigger Using Insulated Gate Bipolar Transistors." *IEEE Trans. Plasma Sci*. 41.4 (2013).

[18] F. W. Grover. *Inductance Calculations*. Mineola: Dover Publications, 2009.

[19] H. A. Wheeler. “Formulas for the Skin Effect.” *Proceedings of the IRE* 30.9 (1942).

[20] M. Margraf. Quite Universal Circuit Simulator. Computer software. Version 0.0.17 2009.

[21] L. Spitzer. *Physics of Fully Ionized Gases*. New York: Interscience, 1962.

Appendix A – Mochi.LabJet.Gun

A.1 Mochi.Labjet.Gun Assembly

PARTS LIST			
ITEM	QTY	PART NAME	SUPPLIER
1	1	Inner Electrode Assembly	In House
2	1	Ceramic Disc	In House
3	1	Outer Electrode Assembly	In House
4	1	Vacuum End Dome	MDC
5	1	Middle Electrode Assembly	In House
6	24	Washer 5/16" ID 1/2" OD	McMaster Carr
7	24	Hex Head Bolt 5/16"-24 x 2.5"	McMaster Carr
8	8	Hex Nut 1/4"-20	McMaster Carr
9	8	Washer 1/4" ID 3/8"OD	McMaster Carr
10	8	Socket Cap Screw #10-32 x 2.25"	McMaster Carr
11	24	Washer 5/16" ID 1/2" OD	McMaster Carr
12	24	Hex Head Bolt 5/16"-24 x 1.875"	McMaster Carr
13	8	Brass Washer 5/16" ID 1/2" OD	McMaster Carr
14	8	Plastic Spacer #10 ID 5/16" OD x 1.875"	McMaster Carr
15	4	Ground Return Bar	In House
16	1	Quick Disconnect 1" Tube 2.75" Conflat	MDC
17	8	Button Head Screw #4-40 x 5/8"	McMaster Carr
18	8	Button Head Screw #10-32 x 5/8"	McMaster Carr
19	1	Inner Electrode High Voltage Connecting Tube	In House

PARTS LIST			
ITEM	QTY	PART NAME	SUPPLIER
20	1	Acrylic Break #1	In House
21	1	Mylar Break	In House
22	1	Acrylic Break #2	In House
23	1	Ground Connecting Plate	In House
24	8	Button Head Screw 1/4"-20 x 3/4"	McMaster Carr
25	8	Button Head Screw #4-40 x 5/8"	McMaster Carr
26	16	Worm Drive Hose Clamp 1/2"	McMaster Carr
27	8	Button Head Screw #6-32 x 1/2"	McMaster Carr
28	1	Inner Electrode Assembly	In House
29	16	High Voltage Coaxial Cable Assembly	In House

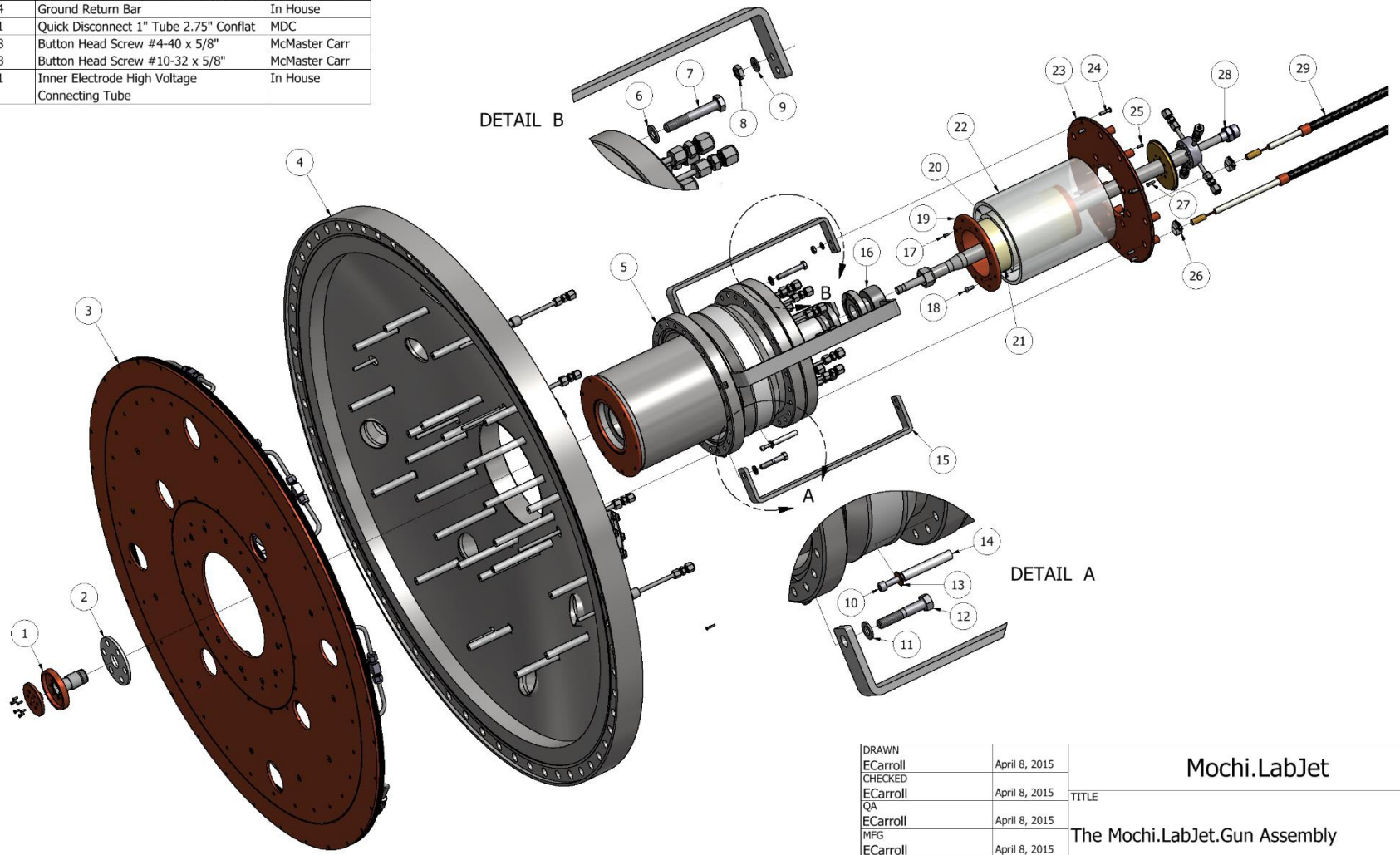

DRAWN	ECarroll	April 8, 2015
CHECKED	ECarroll	April 8, 2015
QA	ECarroll	April 8, 2015
MFG	ECarroll	April 8, 2015
APPROVED	SYou	April 15, 2015

Mochi.LabJet

TITLE: The Mochi.LabJet.Gun Assembly

SIZE: C | DWG NO: Mochi.LabJet.Gun | REV: -

SCALE 1:5 | SHEET 1 OF 1

A.2 Mochi.LabJet.Gun Inner Electrode Assembly

PARTS LIST			
ITEM	QTY	PART NAME	SUPPLIER
1	6	Flat Head Screw 4-40 x 3/8"	McMaster Carr
2	1	Inner Electrode Disc	In House
3	1	Inner Electrode Cup	In House
5	1	Threaded Tube Electrode Connector	In House
6	1	Threaded Tube Electrode Connector Adapter	In House
7	1	Swagelok 1" Comprression Tube Fitting	Swagelok
8	1	Compression Tube Fitting Hex Nut	Swagelok
9	1	Vacuum Tubing 3/4" OD 5/8" ID	MDC
10	1	Vacuum Tubing 1/2" OD 7/16" ID	MDC
11	2	Conical Reducer 1"-3/4"	MDC
12	1	Vacuum Tubing 1"OD 7/8" ID	MDC
13	4	1/4" Compression Tube Union	Swagelok
14	5	Vacuum Tubing 1/4" OD 3/16" ID	MDC
15	1	Inner Electrode Gas Hub	In House
16	1	VCO Tube Fitting 1/2"	MDC

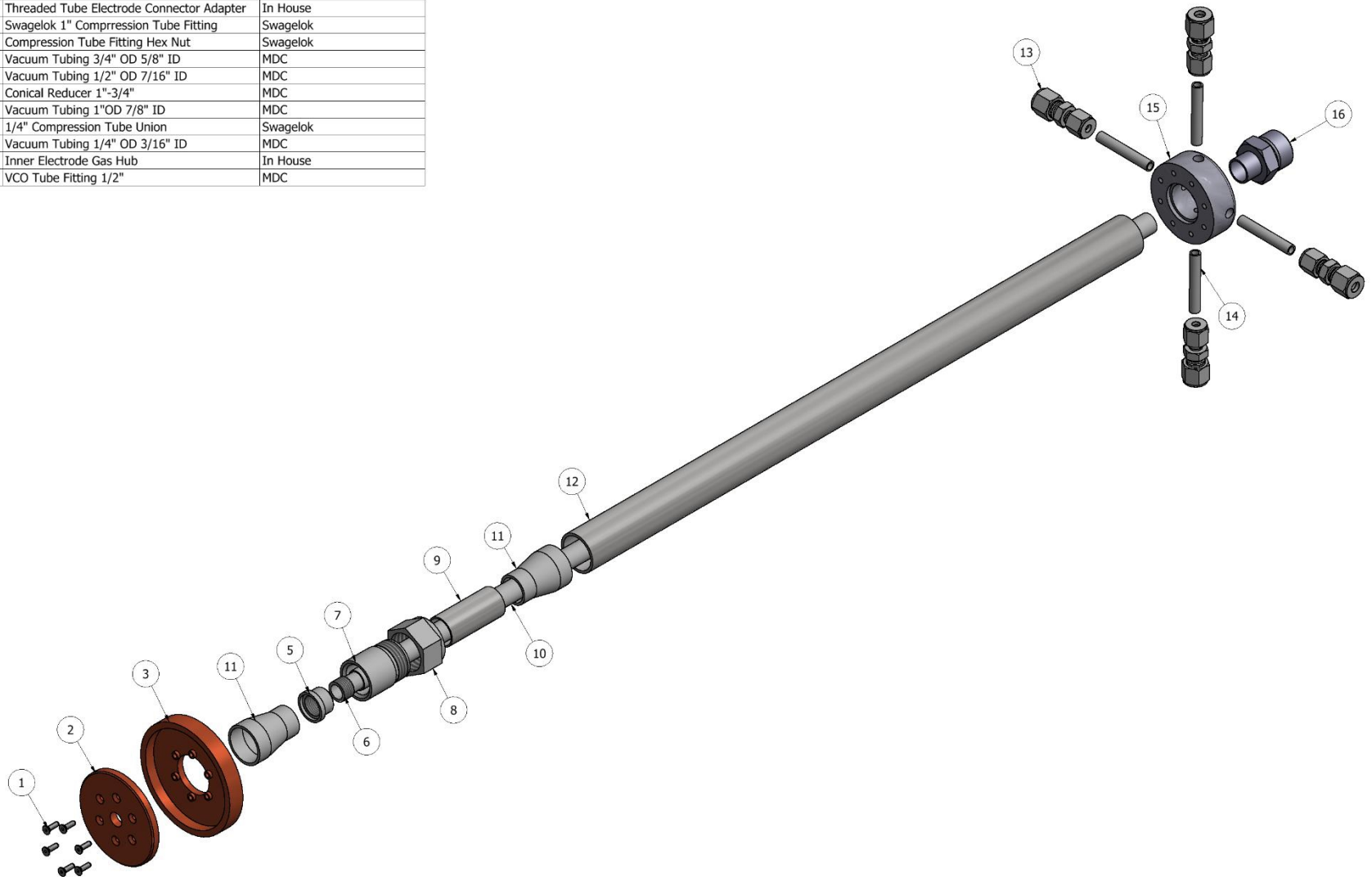

DRAWN ECarroll	April 8, 2015	MOCHI.LabJet	
CHECKED ECarroll	April 8, 2015	TITLE	
QA ECarroll	April 8, 2015	Mochi.LabJet.Gun.InnerElectrode Assembly	
MFG ECarroll	April 8, 2015		
APPROVED SYou	April 15, 2015	SIZE C	DWG NO Mochi.labjet.Gun.InnerElectrode REV -
		SCALE 3:5	SHEET 1 OF 1

A.3 Mochi.LabJet.Gun.MiddleElectrode Assembly

PARTS LIST			
ITEM	QTY	PART NAME	SUPPLIER
1	1	Middle Electrode Ring	In House
2	9	Flat Head Screw #4-40 x 1/2"	McMaster Carr
3	1	Middle Electrode Annulus	In House
4	1	Middle Electrode Backing	In House
5	1	Vacuum Tubing 2.5" OD 2.37" ID	MDC
6	1	Solenoid	Woodruff Scientific
7	1	Conical Reducer 2.5"-1.5"	MDC
8	1	Half Nipple 2.75" CF	MDC
9	1	Ceramic Break 2.75" CF	MDC
10	12	Vacuum Tubing 1/4" OD 3/16" ID	MDC
11	1	Vacuum Tubing 7" OD 6.75" ID	Vita Needle
12	1	Ceramic Envelope 10" CF	MDC
13	12	Compression Tube Reducing Union 1/4"-3/16"	Swagelok

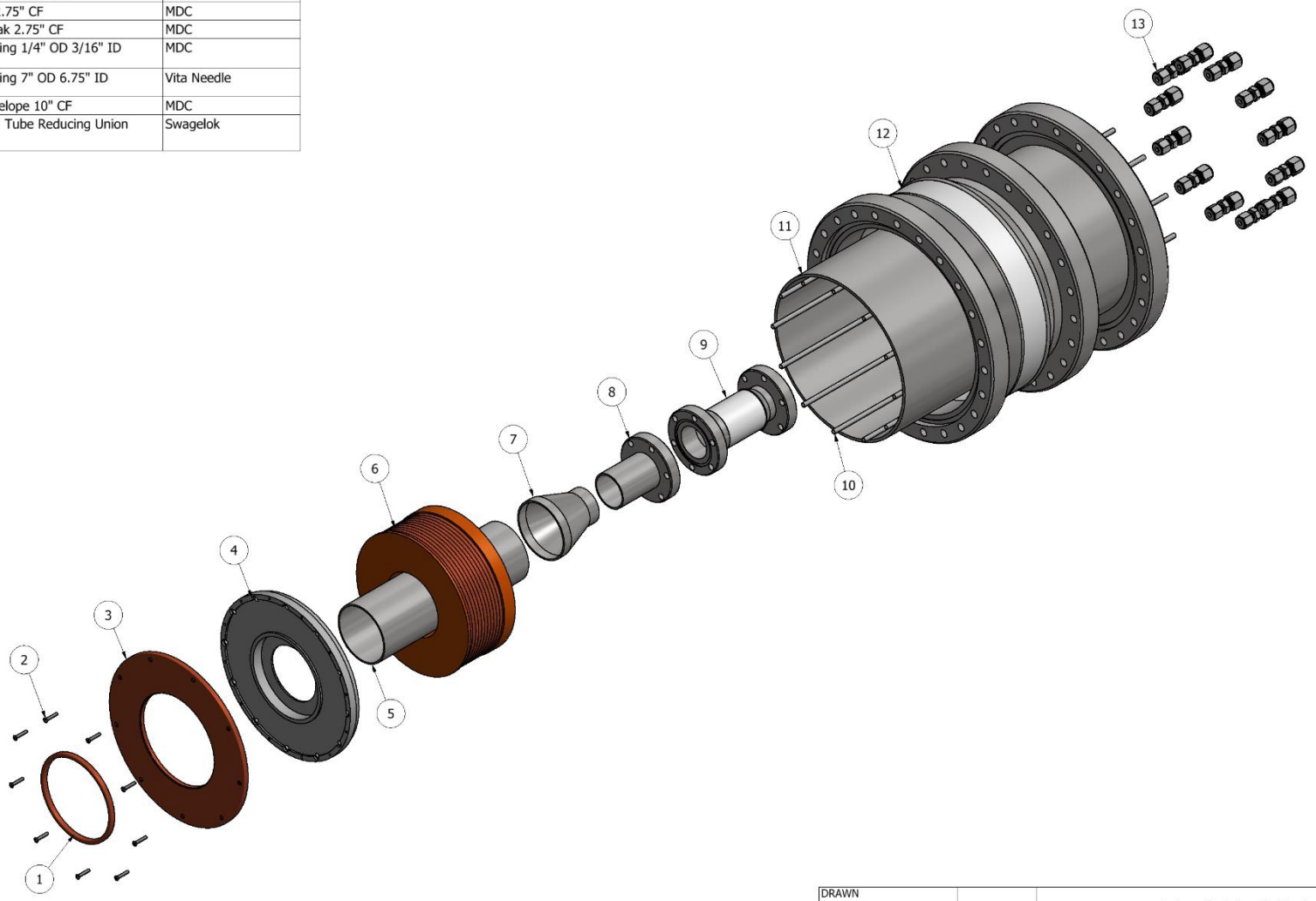

DRAWN ECarroll	April 8, 2015	Mochi.LabJet
CHECKED ECarroll	April 8, 2015	TITLE: Mochi.LabJet.Gun.MiddleElectrode Assembly
QA ECarroll	April 8, 2015	
MFG ECarroll	April 8, 2015	
APPROVED SYou	April 15, 2015	SIZE C; DWG NO Mochi.LabJet.Gun.InnerElectrode; REV -
		SCALE 1:3; SHEET 1 OF 1

A.4 Mochi.LabJet.Gun.Outer.Electrode Assembly

PARTS LIST			
ITEM	QTY	PART NAME	SUPPLIER
1	1	Inner Plenum Assembly	In House
2	1	Outer Plenum Assembly	In House
3	96	#4-40 Hex Nut	McMaster Carr
4	96	#4 Washer	McMaster Carr
5	1	Outer Electrode	In House
6	64	Flat Head Screw #4-40 x 3/4"	McMaster Carr

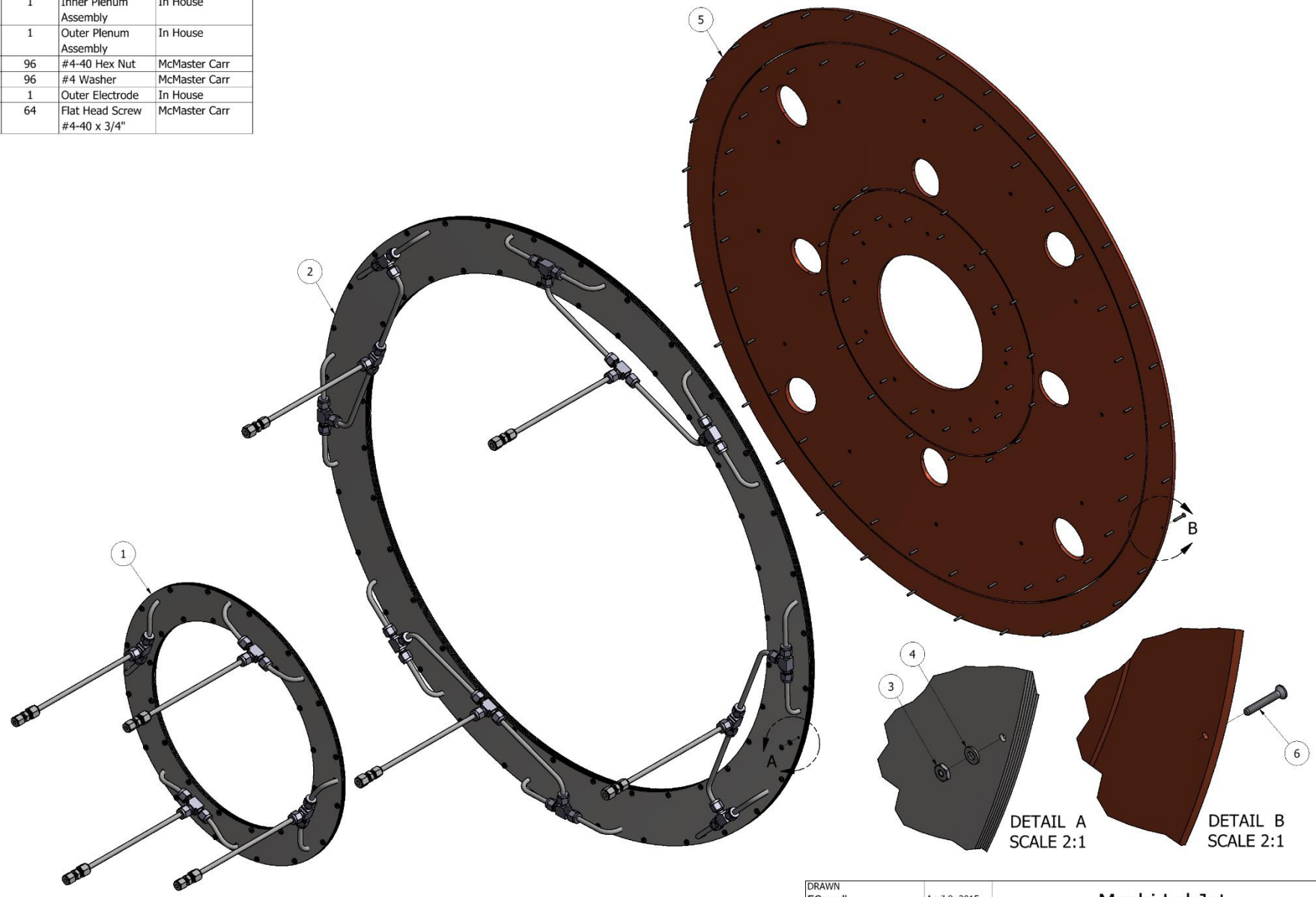

DETAIL A
SCALE 2:1

DETAIL B
SCALE 2:1

DRAWN ECarroll	April 8, 2015	Mochi.LabJet
CHECKED ECarroll	April 8, 2015	TITLE
QA ECarroll	April 8, 2015	Mochi.LabJet.Gun.OuterElectrode Assembly
MFG ECarroll	April 8, 2015	
APPROVED SYou	April 15, 2015	SIZE C / DWG NO Mochi.LabJet.Gun.OuterElectrode / REV -
		SCALE 2:7 / SHEET 1 OF 1

A.4.1 Mochi.LabJet.Gun.OuterElectrode.InnerPlenum Assembly

PARTS LIST			
ITEM	QTY	PART NAME	SUPPLIER
1	1	Inner Plenum Outer Riser	In House
2	1	Inner Plenum Inner Riser	In House
3	4	Inner Plenum Layer	In House
4	4	Inner Plenum Lid	In House
5	1	Fancy Bend Left Tube	In House
6	1	Fancy Bend Right Tube	In House
7	1	Vacuum Tubing 1/4" OD 3/16" ID	MDC
8	1	Compression Tube Union 1/4"	Swagelok

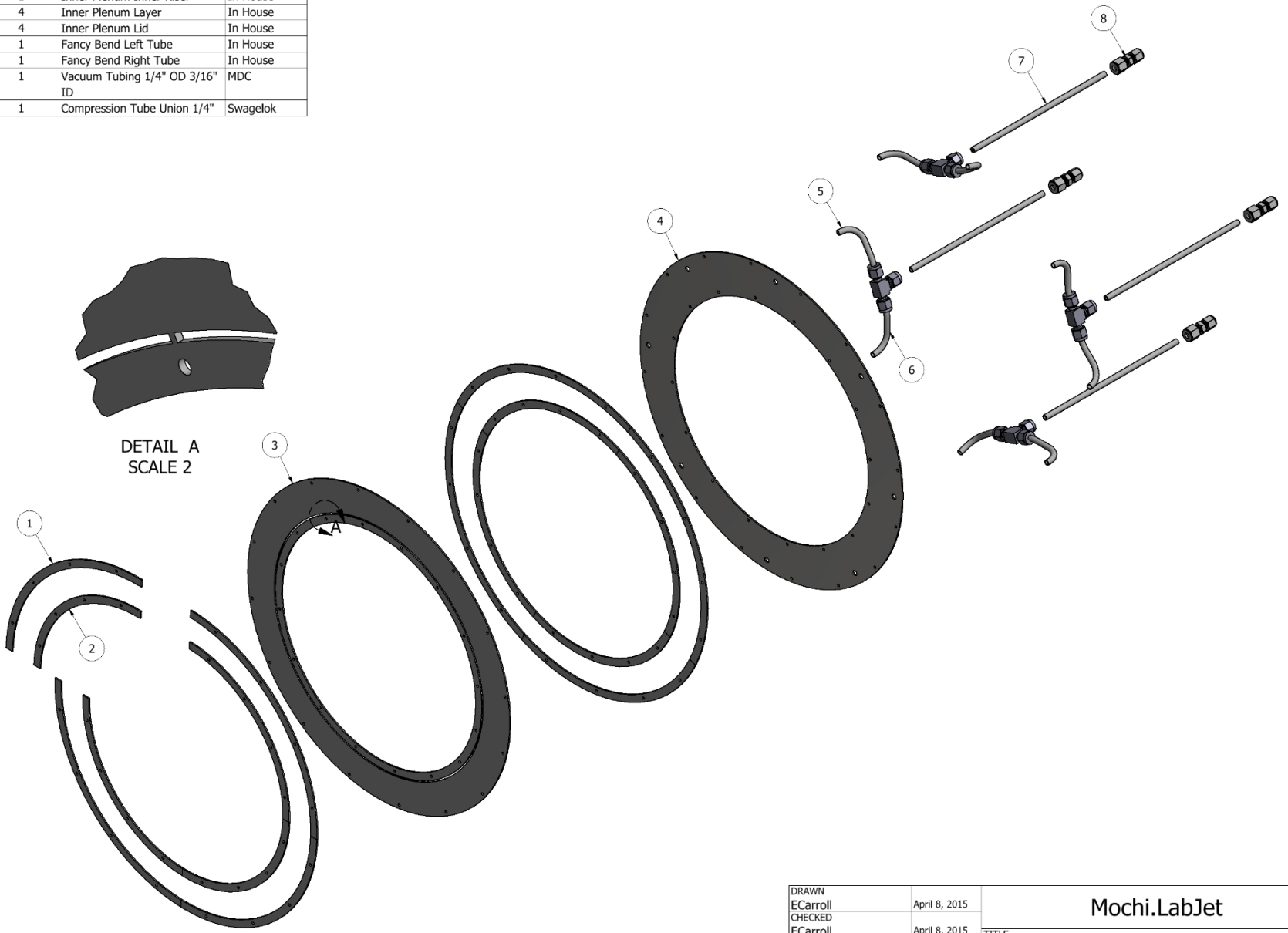

DRAWN ECarroll	April 8, 2015	Mochi.LabJet	
CHECKED ECarroll	April 8, 2015	TITLE	
QA ECarroll	April 8, 2015	Mochi.Labjet.Gun.OuterElectrode.InnerPlenum	
MFG ECarroll	April 8, 2015		
APPROVED SYou	April 15, 2015	SIZE C	DWG NO Mochi.LabJet.Gun.OuterElectrode.InnerPlenum REV -
		SCALE 1:3	SHEET 1 OF 1

A.4.2 Mochi.LabJet.Gun.OuterElectrode.OuterPlenum Assembly

PARTS LIST			
ITEM	QTY	PART NAME	SUPPLIER
1	1	Outer Plenum Outer Riser	In House
2	1	Outer Plenum Inner Riser	In House
3	4	Outer Plenum Layer 1	In House
4	1	Outer Plenum Layer 2	In House
5	1	Outer Plenum Lid	In House
6	1	Header Tube 1	In House
7	1	Header Tube 2	In House
8	1	Compression Tube T 1/4"	Swagelok
9	1	Vacuum Tubing 1/4" OD 3/16" ID	In House
10	1	Compression Tube Union 1/4"	Swagelok

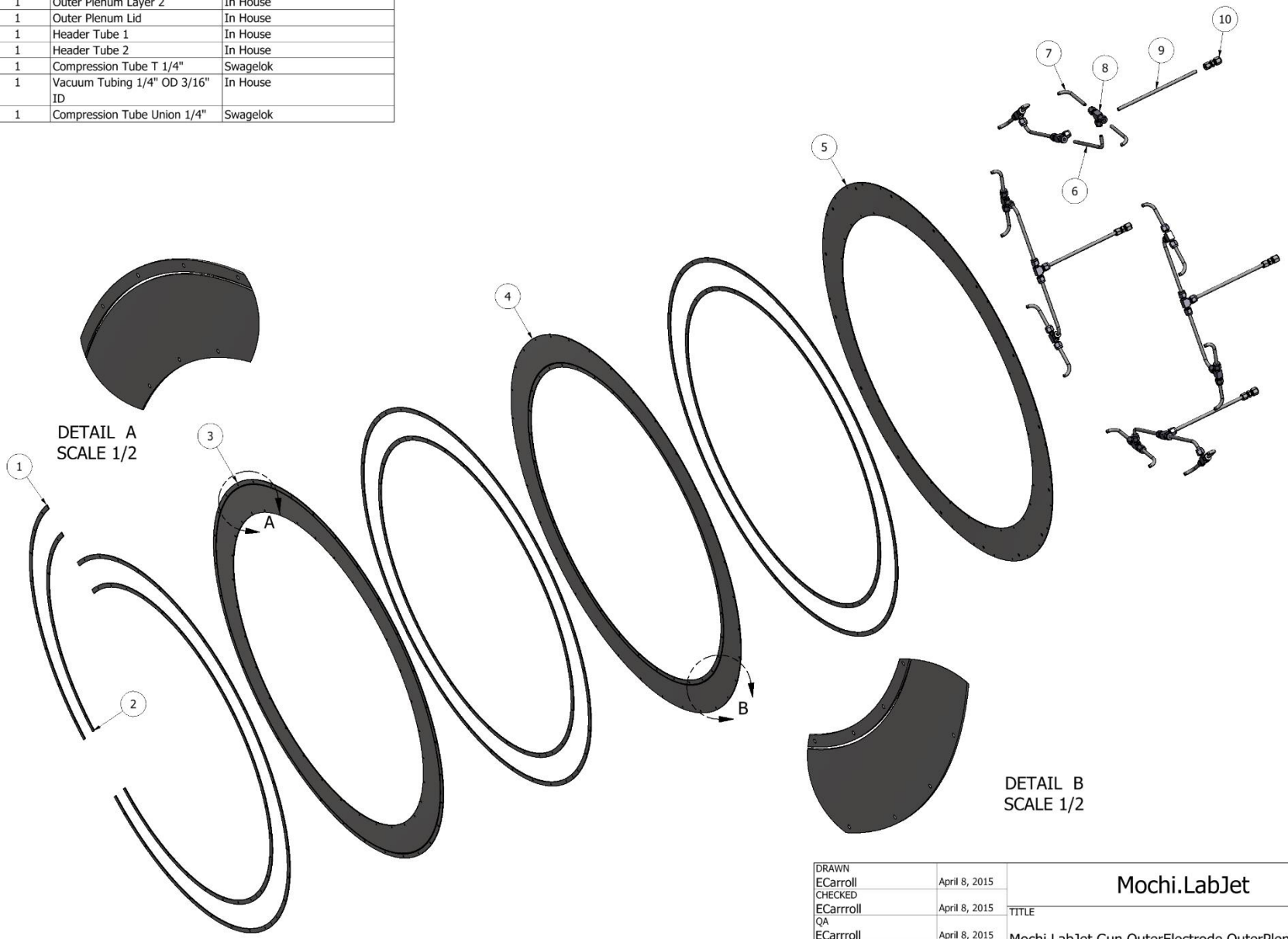

DRAWN ECarroll	April 8, 2015	Mochi.LabJet
CHECKED ECarrroll	April 8, 2015	TITLE: Mochi.LabJet.Gun.OuterElectrode.OuterPlenum Assembly
QA ECarrroll	April 8, 2015	
MFG ECarroll	April 8, 2015	
APPROVED SYou	April 15, 2015	
SIZE C	DWG NO Mochi.LabJet.Gun.OuterElectrode.OuterPlenum	REV -
SCALE 1:6	SHEET 1 OF 1	

Appendix B – Mochi.LabJet.PSU

B.1 Mochi.LabJet.PSU.IgnitronTower

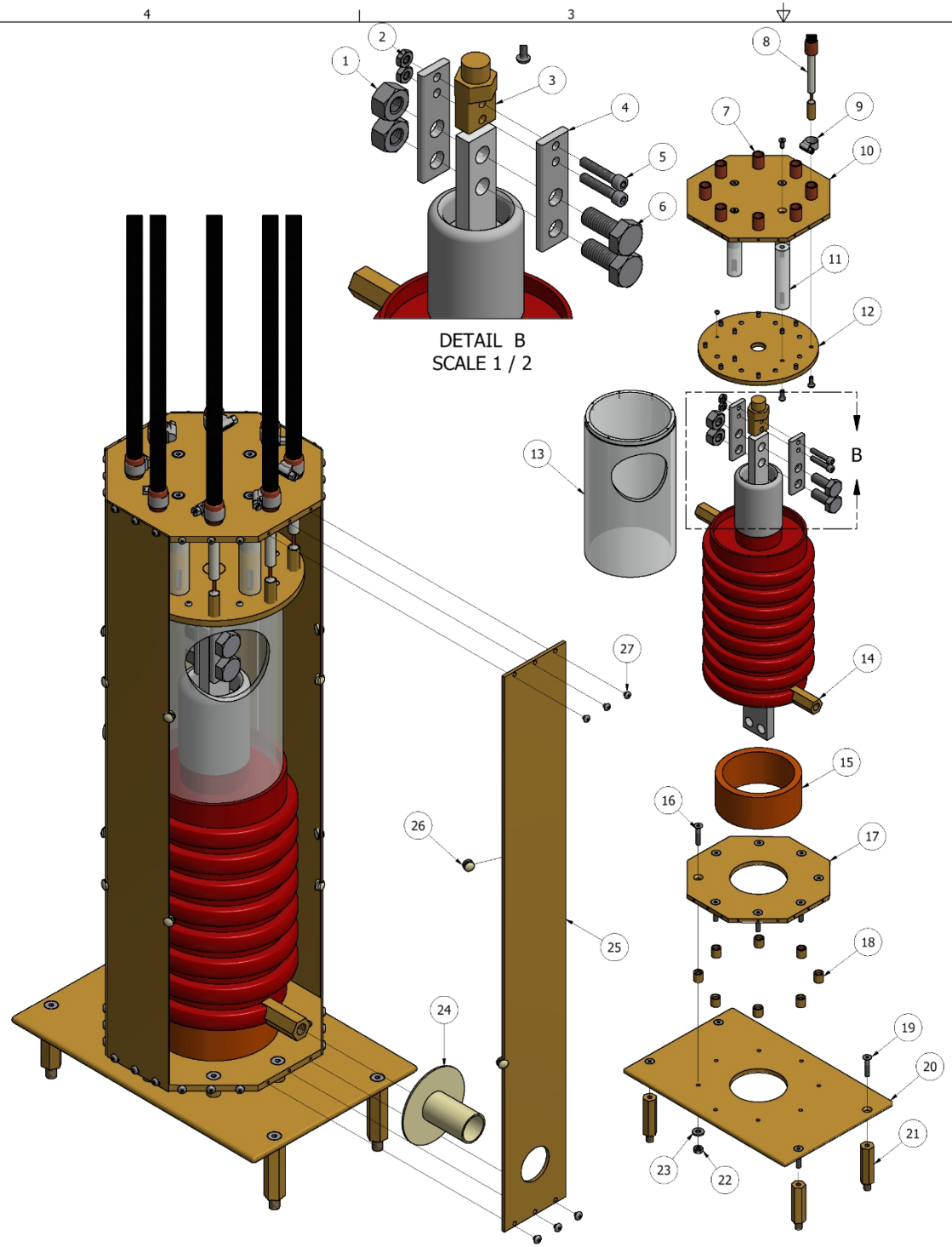

PARTS LIST

ITEM	QTY	PART NAME	SUPPLIER
1	1	Hex Nut 1/2"-13	McMaster Carr
2	1	Hex Nut 1/4"-20	McMaster Carr
3	1	Hex Plug	In House
4	2	Ignitron To Hex Plug Bus Connector	In House
5	1	Socket Cap Screw 1/4"-20 x 1.25"	McMaster Carr
6	1	Hex Bolt 1/2"-13 x 1.5"	McMaster Carr
7	1	Copper Tubing 1/2" OD 3/8" ID	McMaster Carr
8	1	RG-217 Coaxial HV Connector	In House
9	1	Worm Drive Hose Clamp	McMaster Carr
10	8	Upper Return Hex Plate	In House
11	4	Acrylic Standoff	In House
12	6	Hot Connector Plate	In House
13	8	Acrylic Break	In House
14	8	D Ignitron	On Hand
15	8	Phenolic Ring	In House
16	12	Flat Head Screw #10-32 x 1"	McMaster Carr
17	4	Lower Return Hex Plate	In House
18	4	Spacer #10	In House
19	8	Flat Head Screw 1/4"-28 x 1/2"	McMaster Carr
20	8	Return Base Plate	In House
21	8	Base Plate Standoff	In House
22	24	Hex Nut #10-32	McMaster Carr
23	24	Washer #10	McMaster Carr
24	2	Shoulder Washer Nylon	ZaP Lab
25	2	Brass Return Sheet	In House
26	2	Return Sheet Spacer	In House
27	2	Button Head Screw #6-32 x 3/8"	McMaster Carr

DRAWN	ECarroll	Jan 12, 2014
CHECKED	ECarroll	Jan 12, 2014
QA	ECarroll	Jan 12, 2014
MFG	ECarroll	Jan 12, 2014
APPROVED	SYou	Jan 17, 2014

Mochi.LabJet

TITLE

Mochi.Labjet.PSU.IgnitronTower

SIZE	DWG NO	REV
C	Mochi.LabJet.PSU.IgnitronTower	-

SCALE 1:4 SHEET 1 OF 1

B.2 Mochi.LabJet.PSU.CapacitorBank Assembly

PARTS LIST			
ITEM	QTY	PART NAME	SUPPLIER
1	5	120 uF 10 kV Capacitor	General Atomics
2	8	Ground Strap Bus Bar	In House
3	14	Hex Bolt 3/8"-18 x 5/8"	McMaster Carr
4	5	Hex Nut 1/2"-13	McMaster Carr
5	1	Hot Strap Bus Bar	In House
6	2	Hex Nut 1/4"-20	McMaster Carr
7	1	L Connecting Bus Bar	In House
8	2	Socket Cap Screw 1/4"-20 x 3/4"	McMaster Carr
9	2	Hex Bolt 1/2"-13 x 1"	McMaster Carr
10	1	Skull Connector	In House
11	1	Hex Nut 1/4"-20	McMaster Carr
12	2	Hex Nut 1/2"-13	McMaster Carr

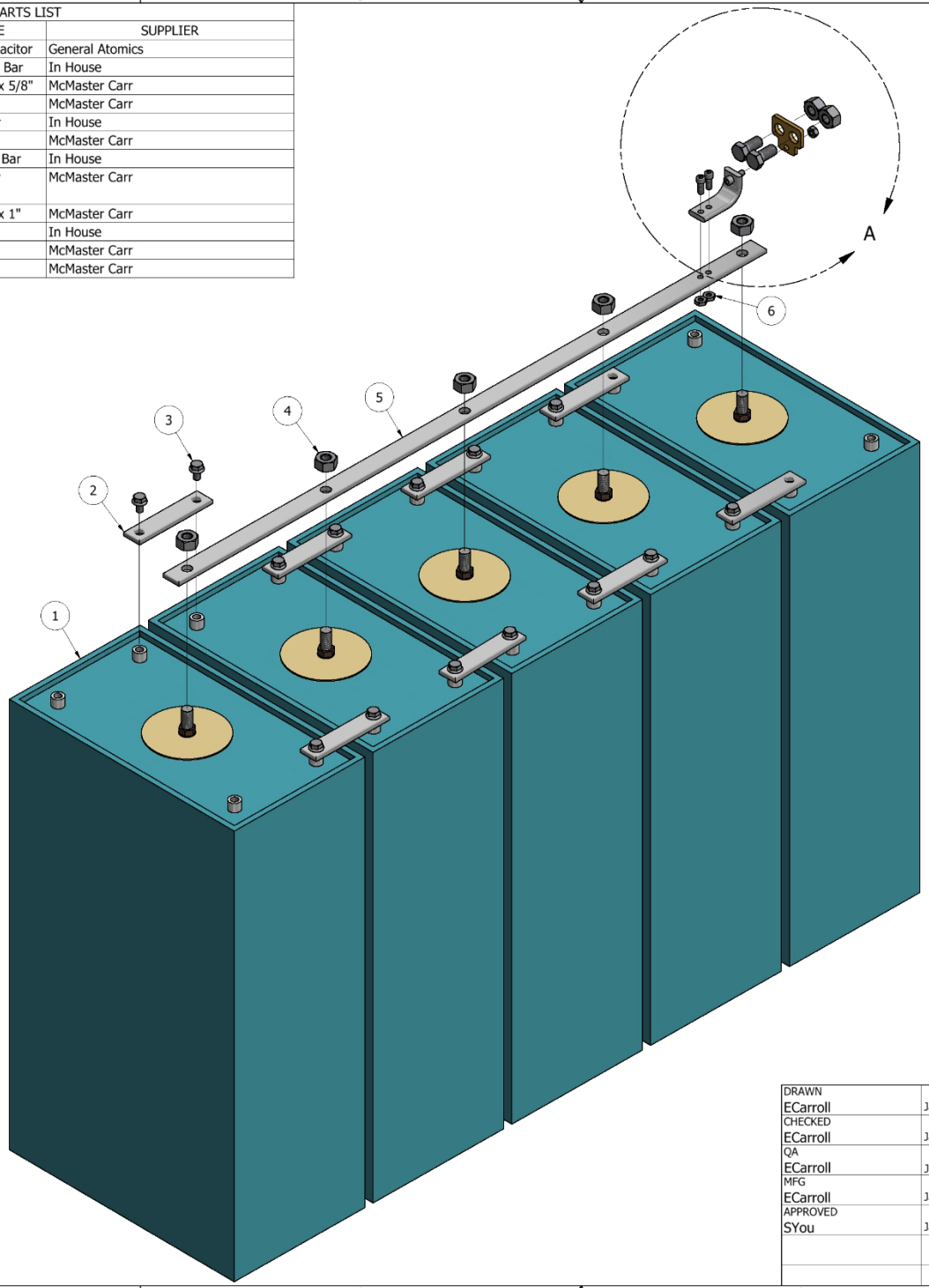

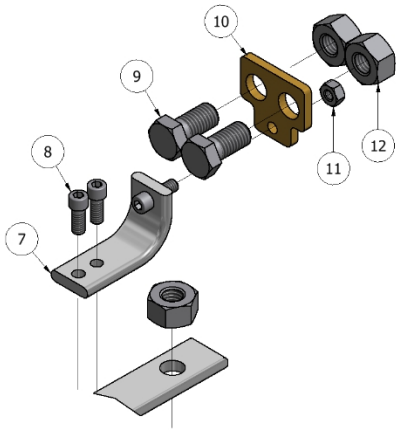

DETAIL A
SCALE 2:1

DRAWN	ECarroll	Jan 12, 2014
CHECKED	ECarroll	Jan 12, 2014
QA	ECarroll	Jan 12, 2014
MFG	ECarroll	Jan 12, 2014
APPROVED	SYou	Jan 15, 2014

Mochi.LabJet

TITLE: Mochi.LabJet.PSU.CapacitorBank Assembly

SIZE: C | DWG NO: Mochi.LabJet.PSU.CapacitorBank | REV: -

SCALE 2:7 | SHEET 1 OF 1